Printing High Ohmic Resistors and Improvement of a Thin Anode for Two-dimensional Floating Strip Micromegas Detectors

Masterarbeit der Fakultät für Physik
der
Ludwig-Maximilians-Universität München

vorgelegt von

Isabel Frank

geboren in Hanau

München, den 14. September 2017

Drucken von hochohmigen Widerständen und Optimierung einer dünnen Anode für zweidimensionale Floating Strip Micromegas Detektoren

Masterarbeit der Fakultät für Physik

der

Ludwig-Maximilians-Universität München

vorgelegt von

Isabel Frank

geboren in Hanau

München, den 14. September 2017

Gutachter: Prof. Dr. Otmar Biebel

Abstract

Micromegas detectors are planar gaseous high-rate capable particle detectors with excellent spatial and temporal resolution. Unlike the standard Micromegas design, floating strip Micromegas use anode strips which are on a floating electrical potential due to high ohmic contact to the high voltage supply. A two-dimensional readout was studied with two layers of readout strips arranged perpendicular to each other. A screen printing method to reliably connect the anode strips individually to high voltage using a high atomic polymer resistive paste was improved. Against bending during detector operation due to gravitational sag the $0.1\,\text{mm}$ thin anode had to be supported with commercial grade aramid fiber paper honeycomb. The described methods resulted in a finalized anode which was used for the completion of a working floating strip Micromegas detector with the optimized thin anode with an active area of $(19.2 \times 19.2)\,\text{cm}^2$. It has been shown that the resistance value, through which the anode strips are individually connected to high voltage, does not affect the pulse height and the timing of detector signals.

Kurzfassung

Micromegas Detektoren sind planare Gasdetektoren, die auch bei sehr hohen Raten Teilchenspuren präzise vermessen können. Anders als Standard Micromegas Detektoren verwenden Floating Strip Micromegas Detektoren Anodenstreifen, die einzeln über hochohmige Widerstände mit Hochspannung verbunden sind. Eine zweidimensionale Auslese wurde durch zwei Lagen senkrecht zueinander angeordneter Auslesestreifen erreicht. Mit Hilfe eines Siebdruckverfahrens wurden die Anodenstreifen über hochohmige Widerstände einzeln mit Hochspannung verbunden. Diese Methode wurde im Rahmen dieser Arbeit weiterentwickelt und verbessert. Um eine Verformung der dünnen Anode wärend des Detektorbetriebes zu vermeiden, wurde sie mit handelsüblichem Aramidfaser-Honeycomb gestützt. Ein Floating Strip Micromegas Detektor mit optimierter dünner Anode und einer aktiven Fläche von $(19.2 \times 19.2)\,\mathrm{cm}^2$ wurde zusammengebaut und in Betrieb genommen. Es wurde gezeigt, dass der Widerstandswert, über den die Anodenstreifen mit Hochspannung verbunden sind, keinen Einfluss auf die Pulshöhe und die Zeitauflösung von Detektorsignalen nimmt.

Contents

Chapter 1

Introduction and Motivation

The MICRO MEsh GASeous (Micromegas) detectors, invented two decades ago by [Giomataris et al., 1996], have undergone an intensive development in recent years. They are high-rate capable, high spatial resolution micro-pattern gaseous detectors, based on parallel plate avalanche chambers.

1.1 The Micromegas Detector

In addition to the standard Micromegas detector, there are two different further developments: First the resistive strips Micromegas detectors which find large-scale application in the ATLAS[1] experiment at the Large Hadron Collider (LHC) of the research center CERN near Geneva in Switzerland. A detailed description of their operation can be found in [Bortfeldt, 2014]. Second, the Floating Strip Micromegas detectors, which are the subject of this thesis.

The functional principle of a standard Micromegas detector is as follows, a schematic is shown in Fig. 1.1: Charged particles or photons traverse the detector and ionize the detector gas in the several millimeters wide drift region between cathode and micro-mesh, producing electron-ion pairs. These electron-ion pairs get separated by an electric field of about 0.8 kV/cm. Electrons drift within 100 ns towards the micro-mesh into the amplification region between mesh and anode, ions towards the cathode. The electrons are accelerated and more electrons are generated by an avalanche process. This process takes place in the amplification region with an electric field of about 39 kV/cm. The electron charge on the readout strips can be detected with preamplifiers. By reading out every strip individually the particle hit position and the timing can be measured precisely.

---

[1]**A T**orodial **L**HC **A**pparatu**S**
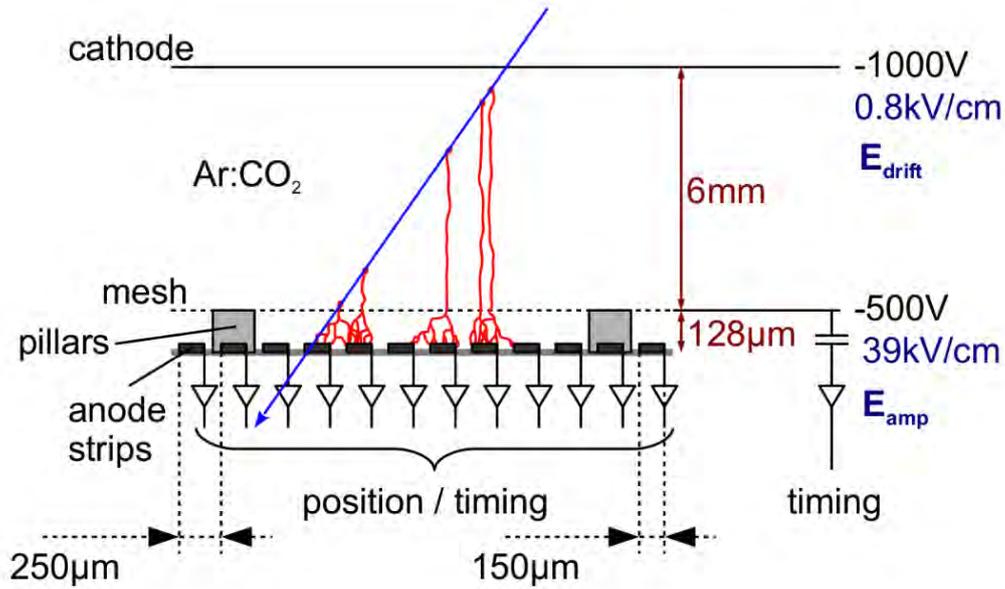
Figure 1.1: Functional principle of a standard Micromegas detector [Bortfeldt, 2014]. The micro-mesh is supplied with high-voltage. An incoming charged particle, represented by the blue line, ionizes the detector gas. The created electrons drift through the micro-mesh and start an electron avalanche due to the high electric field in the amplification region between micro-mesh and anode. The electrons are collected on anode strips and the signal is readout with preamplifiers.

1.2 On the Content of this Thesis

This thesis is focused on the floating strip Micromegas detectors. After introducing the physics on which Micromegas detectors are based on, the mechanical and operational features of a floating strip Micromegas detector are described. Further developed as well as improved methods for completing an optimized thin anode for a two-dimensional floating strip Micromegas detector are presented. Using the screen printing method high ohmic resistors were printed to connect the anode strips individually to high voltage. Finally, it was examined whether these resistances affect the pulse height and the timing of the detector signals.

Chapter 2

Interaction of Particles with the Detector

This chapter introduces the physics on which Micromegas detectors are based on. Starting with the principles of particles interacting with matter, this chapter will discuss the subject of multiple scattering and the behavior of particles in a gas with applied electric field.

2.1 Interaction of Charged Particles with Matter

The mean energy loss of charged particles depends on the material they are interacting with as well as on their energy. This relation is described by the Bethe-Bloch formula [Leo, 1994] which gives the average energy loss per unit length:

$$\left\langle \frac{dE}{dx} \right\rangle = -2\,\pi\,N_\mathrm{A}\,r_\mathrm{e}^2\,m_\mathrm{e}\,c^2 \rho\,\frac{Z z^2}{A\beta^2} \left[\ln\left(\frac{2\,m_\mathrm{e}\,\gamma^2\,v^2\,W_\mathrm{max}}{I^2} \right) - 2\,\beta^2 - \delta - 2\,\frac{C}{Z} \right] \tag{2.1}$$

$$\text{with} \quad \beta = \frac{v}{c}, \quad \gamma = \frac{1}{\sqrt{1-v^2}} \quad \text{and} \quad W_\mathrm{max} \approx 2\,m_\mathrm{e}c^2\beta^2\gamma^2.$$

with classical electron radius $r_\mathrm{e} = 2.817 \cdot 10^{-13}\,\mathrm{cm}$, electron mass m_e, speed of light c, Avogadro's number $N_A = 6.022 \cdot 10^{23}\,\mathrm{mol}^{-1}$ and mean excitation potential I. The absorbing material has an atomic number Z, atomic weight A, and density ρ. δ is the density correction and C the shell correction. The incident particle has a charge of z in the charge unit e and a velocity of v. W_max is the maximum energy transfer to an electron in a single collision.

Depending on the properties of the absorbing material the stopping power can be calculated by $-\frac{1}{\rho}\left\langle \frac{dE}{dx} \right\rangle$. The mean energy loss decreases by $1/\beta^2$ in the low-energy domain for $\beta\gamma \lesssim 1$ and reaches a minimum at $\beta\gamma \approx 4$. Particles within this momentum range are called minimum ionizing particles (MIPs). The mean energy loss of these particles is in the order of $2\,\frac{\mathrm{MeV\,cm}^2}{\mathrm{g}}$ for almost all absorbing materials. In the strongly relativistic range for $\beta \approx 1$, the energy loss increases again due to the logarithmic term of the Bethe-Bloch formula, depending on γ.

Fig. 2.1 shows the stopping power for positive muons in copper as a function of $\beta\gamma$ and their momentum p.
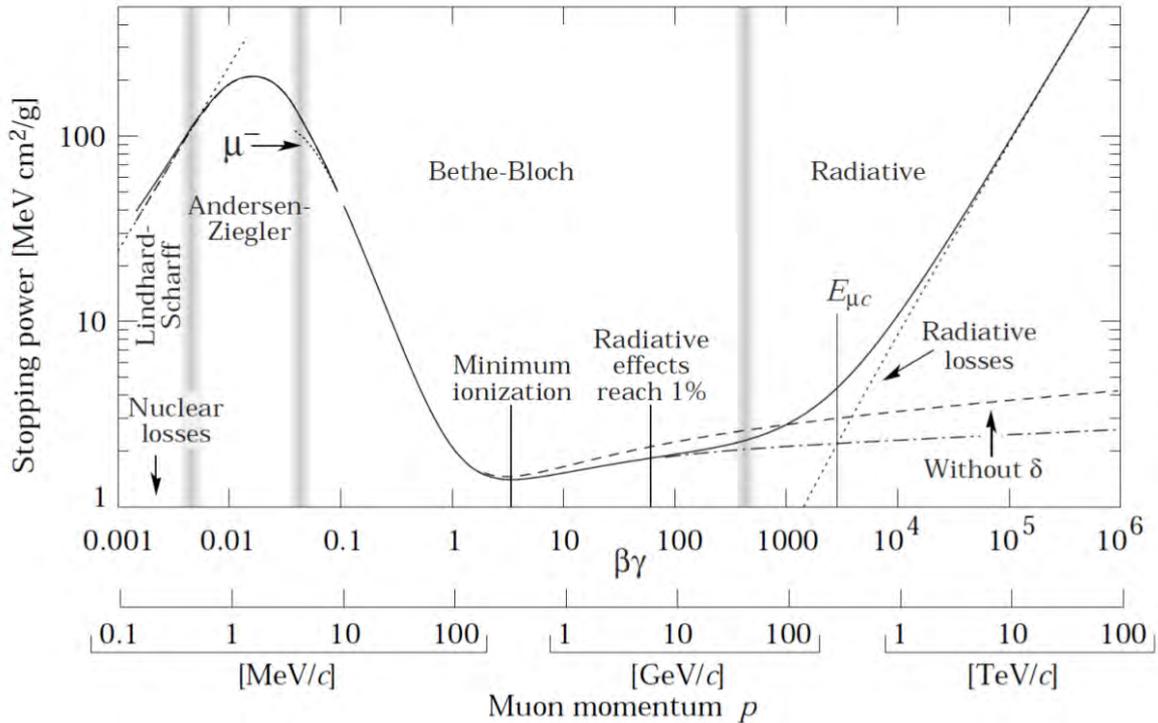
Figure 2.1: Stopping power for positive muons in copper as a function of momentum $p = m\,c\,\beta\,\gamma$ [Groom et al., 2001].

According to [Bichsel, 2006] strong fluctuations around the average energy loss when using thin absorbing materials exist because large amounts of energy are transferred to target electrons. Large energy transfers strongly influence the measured values.

The most probable energy loss of a charged particle in a layer of thickness d can then be described by [Bichsel, 1988, Grupen and Shwartz, 2008]

$$\left.\frac{\Delta E}{\Delta x}\right|_p = 2\,\pi N_{\mathrm{A}} r_{\mathrm{e}}^2 m_{\mathrm{e}} c^2 z^2 \frac{Z}{A}\frac{\rho}{\beta^2}\left[\ln\left(\frac{2\,m_{\mathrm{e}}c^2\beta^2\gamma^2\xi}{I}\right)+0.2\,-\beta^2-\delta\right] \tag{2.2}$$

$$\text{with}\qquad \xi = 2\,\pi N_{\mathrm{A}}\,r_{\mathrm{e}}^2\,m_{\mathrm{e}}\,c^2\,z^2\,\frac{Z}{A}\,\frac{\rho}{\beta^2}\,d\,.$$

2.2   Interaction of Photons with Matter

The interaction of photons with matter is fundamentally different to the interaction of charged particles with matter, as photons do not carry electric charge. There are three different interaction processes of photons with matter, depending on their energy [Kleinknecht, 1992]:

Photoelectric Effect

A photon with an energy of $E_\gamma < 100\,\mathrm{keV}$ can transfer its complete energy to a shell electron and is thereby absorbed. The energy of the electron, which detaches itself from the atomic shell, results from $E_{e^-} = E_\gamma - E_{\mathrm{binding}}$, where E_{binding} is the binding energy of the electron to the atom. If the electron is one of the inner shells, the resulting electron gap is filled through

an electron from a higher shell. Thus the characteristic X-ray radiation of the ionized atom is emitted.

Compton Scattering

A photon with high energy of $E_\gamma = h\nu \gg E_{\text{binding}}$ scatters on an electron and transfers a part of its momentum to that electron. The momentum transmission is angular dependent and maximal at a scattering angle of $180°$.

Pair Production

A photon with more than double the rest energy of an electron of $E_\gamma > 2\,m_e c^2 = 2 \cdot 511\,\text{keV}$ can create an electron-positron-pair in the Coulomb field of a nucleus or a shell electron, where electron and positron obtain the same fraction of kinetic energy $E_{\text{kin}} = \frac{1}{2}(h\nu - 2\,m_e c^2)$.

Fig. 2.2 shows the total cross section of a photon in these processes as a function of the photon energy.
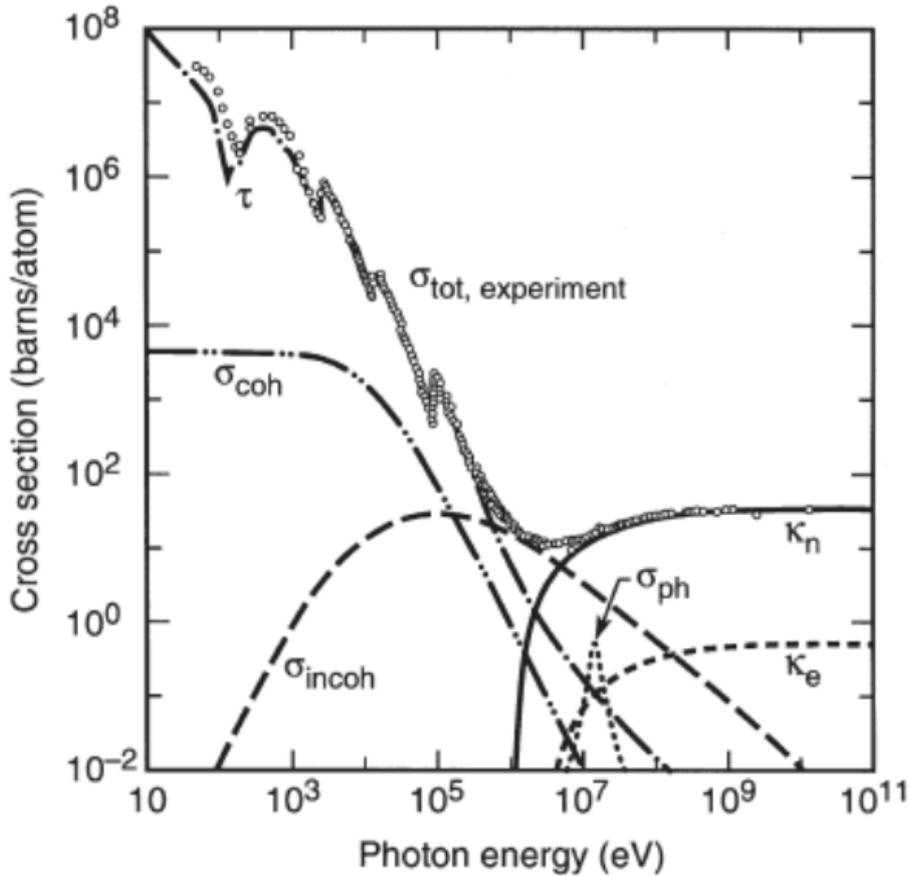
Figure 2.2: Total cross section of photons in lead as a function of the photon energy, combining the individual contributions from photoelectric effect τ, coherent scattering (Rayleigh scattering) σ_{coh}, incoherent scattering (Compton scattering) σ_{incoh}, pair production in the nuclear field κ_{n} and the electron field κ_{e} as well as the nuclear photo absorption σ_{ph} [Hubbell et al., 1980].

2.3 ^{55}Fe Decay

For this thesis a ^{55}Fe source is used in several measurements presented in chapter 6.
The ^{55}Fe isotope decays by electron capture to ^{55}Mn:

$$^{55}_{26}\text{Fe} + e^- \longrightarrow {}^{55}_{25}\text{Mn}^* + \nu_e.$$
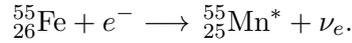
In this process, an electron of the atomic K shell is captured by the nucleus, resulting in a
proton and an electron transform into a neutron and neutrino:

$$p + e \longrightarrow n + \nu_e.$$
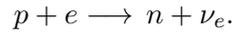
The resulting electron gap is mainly filled by an electron from the higher L shell where a
characteristic X-ray photon with an energy of $E_\gamma = h\nu$ is emitted. The emitted photon
with an energy of $5.9\,\text{keV}$ is dominantly interacting with the atoms of the detector gas by
the photoelectric effect. The photon transfers its total energy to the electron, whereby the
energy of the electron with $E_{e^-} = E_\gamma - E_{binding}$ is known.

2.4 Multiple Scattering of Charged Particles

Multiple scattering occurs when charged particles pass trough matter and undergo multiple
Coulomb interactions. Due to numerous small scatters with matter their directions of flight
are altered. The track of particles propagating through several layers of material can therefore
be kinked. This is an undesired behavior for the reconstruction of the hit position in precise
track detectors, like Micromegas detectors.
The width of the distribution of track inclinations θ_0 is given by [Grupen and Shwartz, 2008]

$$\theta_0 = \frac{13.6\,\text{MeV}}{\beta\,c\,p}\,z\,\sqrt{\frac{x}{X_0}}\left[1 + 0.038\ln\left(\frac{x}{X_0}\right)\right] \qquad \text{with} \qquad \beta = \frac{v}{c}, \qquad (2.3)$$

with velocity v, momentum p and charge z of the scattered particle. x/X_0 describes the
thickness of the absorbing material in units of the radiation length X_0, which is defined
as length of electron energy decrease down to a fraction of $1/e$ from the initial energy via
bremsstrahlung.

For a composition of layered materials with different radiation lengths X_0^i, the resulting
radiation length X_0 can be calculated by

$$X_0 = \frac{1}{\sum \eta_i/X_0^i}, \qquad (2.4)$$

where η_i is the atomic mass fraction of the absorbing material with radiation length X_0^i.

2.5 Drift of Electrons and Ions

In a static electric field electrons and ions move in opposite directions depending on their charge. The mean drift velocity of ions v_{drift} in a gas is given as a function of the electric field

$$v_{\text{drift}} = \mu^+ E \frac{p_0}{p} \,, \tag{2.5}$$

with normal pressure of $p_0 = 1013\,\text{mbar}$, gas pressure p, electric field E and mobility of ions μ^+ [Kleinknecht, 1992]. Tab. 2.1 shows some mobilities of ions used in possible detector gas mixtures of $\text{Ar}:\text{CO}_2$ or $\text{Ne}:\text{CF}_4$ for Micromegas detectors.

The drift of electrons is more complicated. The electrons can gain a lot of energy in the electric field so quantum mechanical processes and elastic scattering become important [Kleinknecht, 1992]. Adding a quencher like CO_2 or CF_4 to the detector gas introduces inelastic scattering of electrons. This increases the effective electron drift velocity. The quencher gas' broader excitation energy spectrum prevents discharges in the detector by prohibiting the formation of streamers. Furthermore, the quencher gas absorbs UV photons created in the gas amplification region. Such photons could ionize the gas creating further charges not correlated to the primary incident particle and therefore disturb the measurement.

gas	ion	mobility μ^+ [$\text{cm}^2\,\text{V}^{-1}\,\text{s}^{-1}$]
Ar	Ar^+	1.54
Ne	Ne^+	4.7
CO_2	CO_2^+	1.09

Table 2.1: Ion mobility in various gases at $1013\,\text{mbar}$ and $20\,°\text{C}$ [Ellis et al., 1976].

2.6 Gas Amplification

The amount of charge created by minimal ionizing particles in gaseous detectors is rather small. To get a sufficiently amount of charge which is observable on the readout electronics of the detector, a process of charge multiplication is required. In a high electric field electrons can be strongly accelerated and thus gain sufficient energy to further ionize gas atoms in collisions. This process is called avalanche multiplication or gas amplification. The number of electrons $\mathrm{d}n$ created in an avalanche is given by

$$\mathrm{d}n(x) = \alpha\, n\, \mathrm{d}x \tag{2.6}$$

per unit path length $\mathrm{d}x$, where n is the number of primary electrons. The inverse of the mean free path λ of free electrons in the gas describes the number of electrons additionally generated by collision processes per length and is called the first Townsend coefficient: $\alpha = \lambda^{-1}$.

Integration yields

$$n(x) = n_0 \cdot \mathrm{e}^{\alpha x} = G \cdot n_0 \,. \tag{2.7}$$

The factor G describes the multiplication factor of charges, so-called gas gain. It is determined as the ratio of the electrons produced after the gas amplification to primary electrons:

$$G = \frac{n}{n_0} = \mathrm{e}^{\,\alpha x} \, .$$

(2.8)

This coefficient α is gas specific, depending on the electric field, gas pressure and temperature [Kleinknecht, 1992].

Chapter 3

Floating Strip Micromegas Detector

This chapter describes the mechanical and operational features of a floating strip Micromegas detector. The technology is based on the standard Micromegas detector which was mentioned in chapter 1. First the functional principle is discussed, followed by the explanation of signal formation, mesh transparency and the discharges between anode and micro-mesh. Furthermore, a two-dimensional readout floating strip structure is introduced.

3.1 Functional Principle of a Floating Strip Micromegas Detector

The functional principle of the floating strip Micromegas, shown in Fig. 3.1, is similar to the standard Micromegas detector. Charged particles traverse the detector and ionize the detector gas. The created electrons drift into the high-field region between micro-mesh and anode strips, where they are amplified into Townsend avalanches.

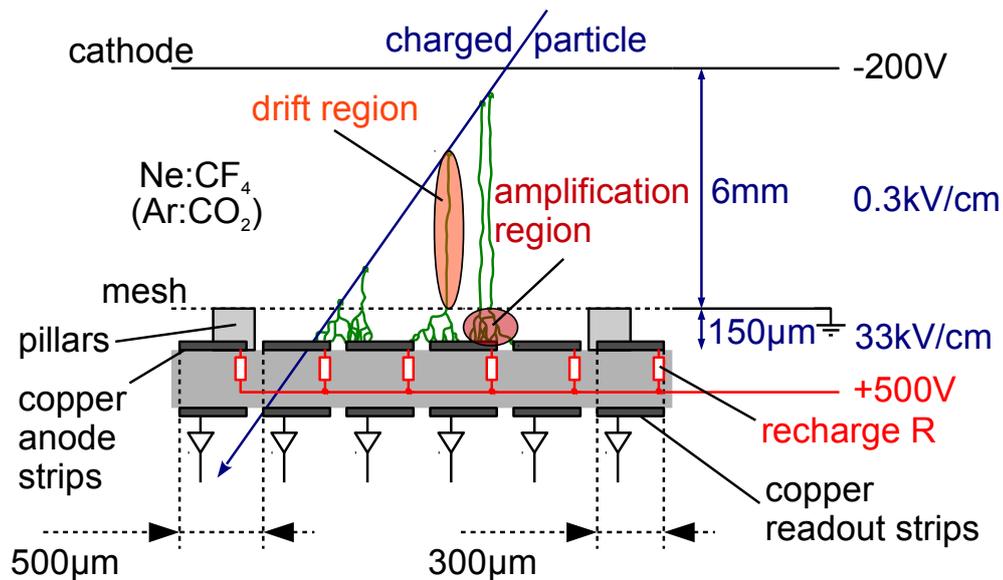Figure 3.1: Schematic and functional principle of a floating strip Micromegas detector [Klitzner et al., 2016]. A charged particle ionizes the detector along the blue line. The generated electrons drift to the mesh and enter the amplification region where they generate a Townsend avalanche. The charge signal is capacitively coupled to the readout strips which are separated by a thin Kapton layer from the anode strips.

The anode readout structure of a floating strip Micromegas detector typically consists of photo-lithographically etched copper strips with a width of 150 µm and a pitch of 250 µm on a printed circuit board (PCB). Unlike the standard Micromegas design the readout strips are beneath these anode strips which are on a floating electrical potential due to high ohmic contact to a high voltage (HV) supply. They are individually connected to high voltage via high ohmic resistors of 20 MΩ [Bortfeldt, 2014]. The resistors are made by use of the screen printing method: A high ohmic polymer resistive paste mixture with different resistivity is printed onto the anode. This allows for a smaller strip pitch compared to standard Micromegas detector resistors and avoids the time consuming soldering process. The screen printing method is described in detail in the following chapter.

The charge signal is capacitively coupled to parallel copper readout strips below the anode strips which are separated by a thin Kapton layer, each forming a high voltage resistant capacitor. The signal on every strip is then further amplified and shaped by an APV25[1] chip [French et al., 2001]. The advantage of a Micromegas detector is the fast signal generation and its fast propagation to the readout electronics, which is in the order of 100 ns, making the detector high-rate capable.

The micro-mesh is held at a constant distance of 150 µm to the anode, realized by a 150 µm high pillar-shaped spacer structure, which is photo-lithographically produced on the anode strips with a pitch of 0.5 mm and a width of 0.3 mm. Unlike the standard Micromegas design, the micro-mesh is grounded (compare Fig. 1.1 and Fig. 3.1). The detector is filled with a gas mixture of a noble gas like Argon (Ar) or Neon (Ne) and Carbon Dioxide (CO_2) or Tetrafluoromethane (CF_4).

3.2   Signal Formation

The formation of signals in Micromegas has been discussed in detail by [Bortfeldt, 2010], the main aspects are described next. Traversing charged particles ionize the detector gas and create electron-ion pairs in the typically 6 mm wide drift region between cathode and micro-mesh, shown in Fig. 3.1. Those pairs are separated by an electric field of about $E_{\mathrm{drift}} = 0.3\,\mathrm{kV/cm}$, the electrons drift within 100 ns towards the amplification region between micro-mesh and anode strips, see section 2.5.

Upon entering the amplification region the electrons are accelerated due to a much higher electric field of about $E_{\mathrm{amp}} = 33\,\mathrm{kV/cm}$ and multiplied in an avalanche process, resulting in charge amplification by a factor in the order of 10^3, described in section 2.6. Due to the large electron mobility, electrons created in this amplification process will reach the anode in less than 1 ns. The much heavier ions drift slowly towards the mesh.

The positive ion cloud, drifting away from the anode strips, induces localized, negative mirror charges on the anode strips and prevents the detection of the electron charges on the preamplifier. By drifting towards the mesh the induced mirror charges vanish, thus releasing the negative electron signal for detection on the preamplifier. With the constant drift of the ions away from the anode strips, the negative charge signal on the anode evolves until the ions reach the mesh. The usual drift time of the ions is about 100 ns. Fig. 3.2 shows the charge configuration after the gas amplification has finished.

---

[1]In this thesis, an APV25 (Analogue Pipeline Voltage mode) has been used for the readout of the floating strip Micromegas detectors. It allows processing of up to 128 strips simultaneously. It is developed for the readout of the CMS tracker at the LHC in CERN [French et al., 2001].

The maximum signal duration is defined by

$$t_{signal} = t_{ion \to mesh} + t_{electron \to abode} \,, \qquad (3.1)$$

$$\text{with} \qquad t_{ion \to mesh} \approx 100 \, ns \qquad \text{and} \qquad t_{electron \to anode} \approx 100 \, ns \,.$$
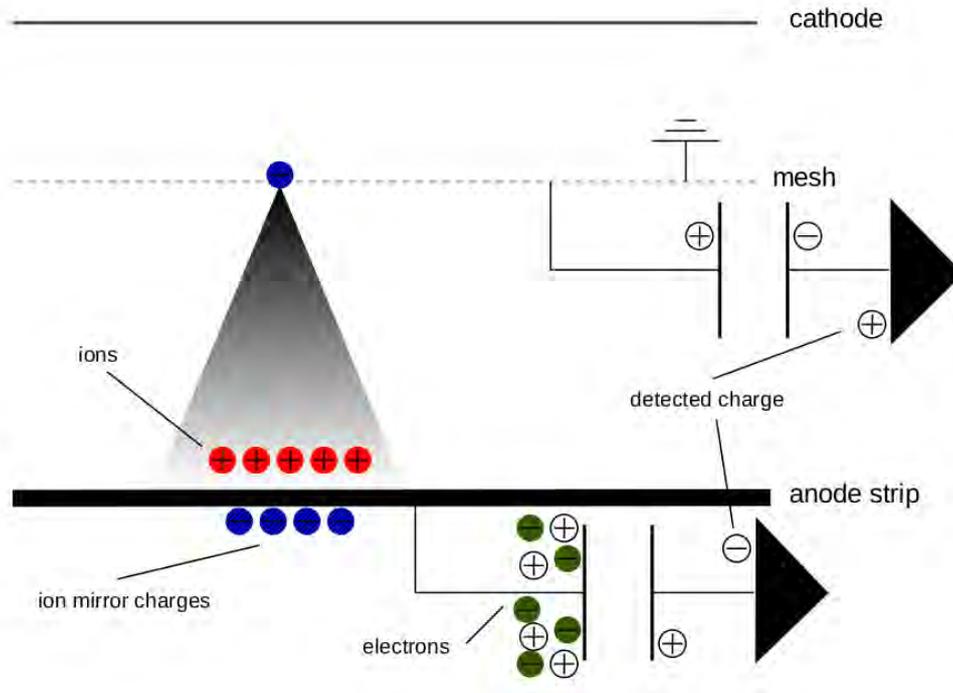

Figure 3.2: Charge configuration in a Micromegas detector after finishing the gas amplification process. Electrons on the anode strips can only be measured after ions have reached the mesh. Figure taken from [Klitzner, 2016b].

3.3 Mesh Transparency

As the electric field in the drift region between cathode and mesh increases, the field line density of the drift field will also increase. Due to the increasing field line density, more field lines reach the mesh. Electrons which are generated in the drift field move along these field lines towards the mesh and do not enter the amplification region. The electron transparency of the mesh, shown by [Giomataris et al., 1996], depends on the ratio of electric field to both sides of the mesh:

$$\xi = \frac{E_{amp}}{E_{drift}}. \qquad (3.2)$$

For a low ratio ξ the electric field lines end on the micro-mesh, the electron can not enter the amplification region, resulting in a low mesh transparency. For a high ratio ξ, the field lines of the drift region get bend through the holes of the mesh into the amplification region, allowing the electrons to reach the amplification region. Due to collisions with the atoms of the detector gas during the drift, the electrons are deflected laterally. This results in a distribution of the electrons upon their arrival at the mesh, as a result of which electrons also hit the mesh and do not reach the amplification region. A large drift field increases the transversal diffusion of the electrons.

3.4   Discharges

Discharges caused by a traversing heavy ionizing particle can spawn a conductive plasma between mesh and anode structure, called streamer [Raether, 1964, Raizer, 1991]. While restoring the potential, no charge amplification is possible. This causes a dead time and makes the detector inefficient.

For standard Micromegas detectors high voltage is applied to the mesh, whereby on discharges the entire detector is deactivated, until the mesh is recharged. In case of floating strip Mircomegas detectors the anode strips are individually connected to high voltage via high ohmic resistors and the mesh is grounded, resulting in only a few strips being affected by local formations of discharges. The rest of the detector remains effective. Additionally since not the whole detector needs to be recharged the dead time for the affected location is also drastically reduced [Bortfeldt, 2014]. The inefficiency $\not\epsilon$ of a floating strip Micromegas detector can be calculated with

$$\not\epsilon = \left(1 - \lambda\,\mathrm{e}^{-\lambda}\right)c\,,\tag{3.3}$$

where c is the fraction of the active area affected by the discharge and $\lambda = t_{\mathrm{dead}} \cdot f_{\mathrm{discharge}}$ with dead time t_{dead} and the discharge rate $f_{\mathrm{discharge}}$. It was shown that

$$\not\epsilon_{\mathrm{floating}} < \frac{1}{1000}\not\epsilon_{\mathrm{standard}}$$

proving the high rate capability of floating strip Micromegas detectors [Bortfeldt, 2014].

3.5   Medical Application of Floating Strip Micromegas Detectors

One field for applications of floating strip Micromegas detectors is in medicine, for example ion transmission tomography. In ion-beam therapy, a beam of protons or carbon ions is used for tumor radiation in the human body. Unlike conventional X-ray radiation, it has a considerable energy loss within a narrow range, the so-called Bragg peak. This allows irradiation of the tumor under protection of the healthy and partially critical tissue around the tumor. For this purpose it is necessary to know the exact position of the tumor in the body, as well as the penetration depth and the course of the beam through the patient. The position of a tumor is usually determined by computer tomography (CT) prior to irradiation, but in the future it is also intended to be determined by means of imaging methods using Micromegas detectors. Therefore, a floating strip Micromegas detector is considered to be installed in front and behind the patient. With this setup it is possible to locate the tumor and determine the beam profile as a result of that. The energy loss in the patient can be determined my measuring the energy of the ions or protons in front and behind the patient. The ion beam radiation therapy offers the great advantage of lower radiation exposure than with conventionally used X-ray radiation therapy. The radiation dose can be deposited in a much more targeted manner by means of the good focus and controllability around the specific energy loss behavior of ions.

3.6 Two-Dimensional Floating Strip Readout Anode

In order to reconstruct two-dimensional hit positions of particles with one single detector, a floating strip Micromegas detector with a two-dimensional readout anode was studied. The signal on the anode strips is coupled to two layers of readout strips, located below the anode strips. There are two possible configurations for this setup: A readout layer orthogonal to the anode strips (y layer) and a parallel readout layer (x layer), placed below the y layer, separated by a 25 µm thin insulating Kapton layer, shown in Fig. 3.3. The readout strips have a width of 0.4 mm and a pitch of 0.5 mm. For the other configuration the order of the parallel and the perpendicular layer is reversed.

Measurements have been shown that the first configuration has a better pulse height ratio between both readout layers [Klitzner et al., 2016], which is why this configuration was used during this thesis.
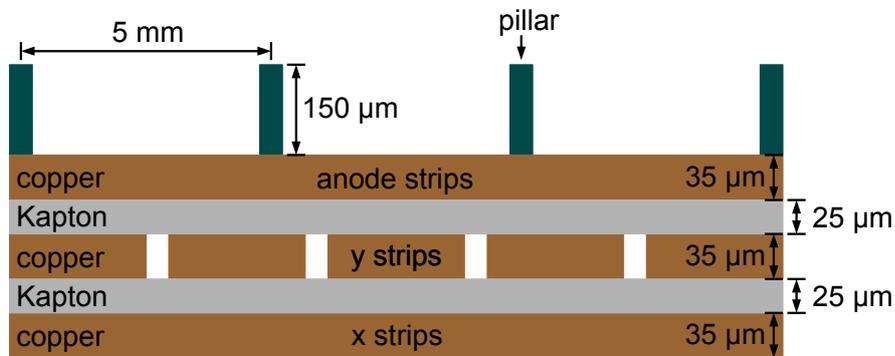

Figure 3.3: Configuration of a floating strip Micromegas detector with two-dimensional readout structure. The signal on the anode strips is coupled to two layers of readout strips, located below the anode strips: A readout layer orthogonal to the anode strips (y layer) and a parallel readout layer (x layer), placed below the y layer, separated by a 25 µm thin insulating Kapton layer.

Chapter 4

Printing High Ohmic Resistors for a Thin Two-Dimensional Floating Strip Micromegas Detector

Unlike standard Micromegas detectors, as described in the introduction, the anode strips of floating strip Micromegas detectors have to be individually connected to high voltage (HV) via high ohmic resistors of about 20 MΩ.

Soldering SMD resistors between the anode strips and HV contact is one way to connect them. The resistances are exactly known and identical for each anode strip. Small dimensions and the number of 384 strips make this process very cumbersome and time consuming. Furthermore, the PCB material with a thickness of 100 µm has limited resistance against high temperature during soldering. Thus, a more efficient method of applying resistors needs to be found. In this thesis a screen printing method with a high ohmic polymer resistive paste by ESL [ESL, 2017] was investigated. This resistive paste has either 100 kΩ/sq or 1 MΩ/sq and is applied between the anode strips and HV contact. Determining the appropriate paste mixture is presented in section 4.4.1. The schematic of the printed resistors is shown in Fig. 4.1. 384 anode strips with a width of 0.2 mm and a pitch of 0.5 mm are located on the PCB, arranged in groups of 16 strips per group. This yields 24 groups on the PCB.
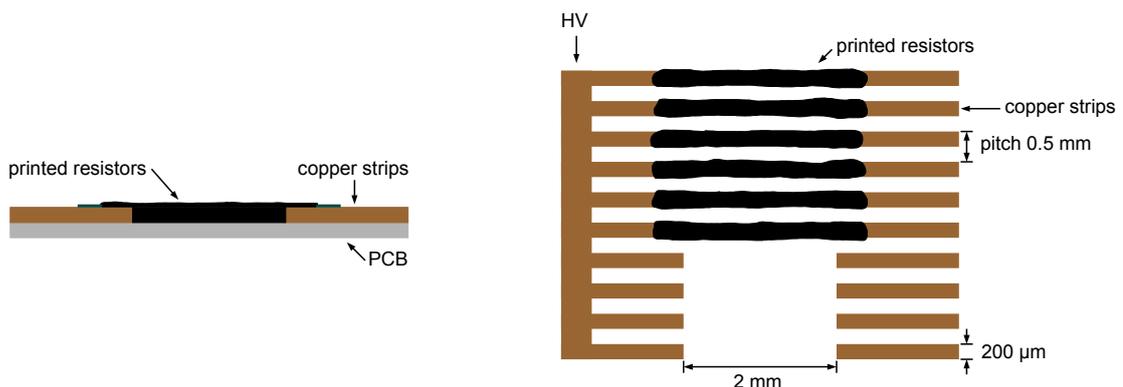

Figure 4.1: Schematic of the printed resistors when using a high ohmic resistive paste to connect the anode strips individually to HV.

After applying the paste onto the PCB it has a low viscosity hence it does not stay in the desired position. Before curing it slowly dissolves across the PCB and connects all strips. Therefore a support structure is required to keep the paste in place. This support structure is made of a solder resistant material, Pyralux PC1025 by DuPont [DuPont, 2017], with a thickness of 64 μm. The schematic of the support structure is shown in Fig. 4.2 (left) and the printed resistors inside the support structure in Fig. 4.2 (right).
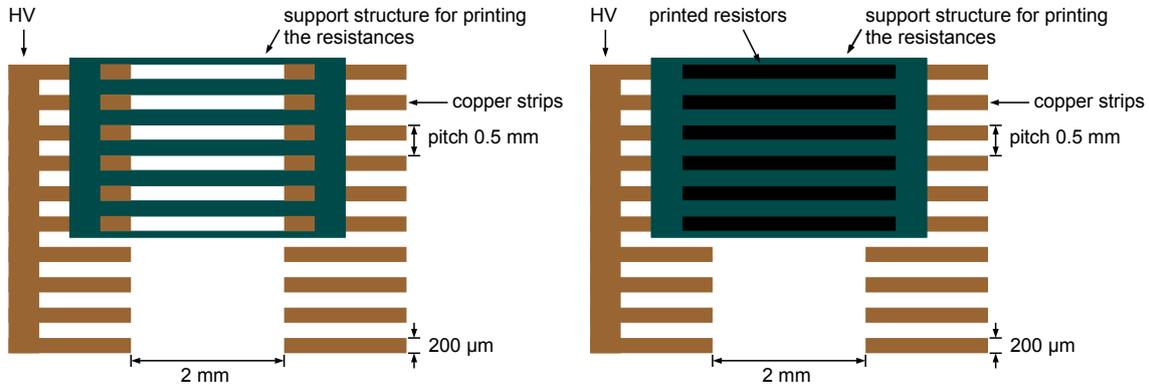

Figure 4.2: Schematic of the screen printing method when using a support structure. First, a support structure is created out of a solder resist material (left). Afterwards the paste can be printed into the gaps of the support structure (right). Each anode strip is individually connected to HV because the paste can not dissolve while still being supported by this structure.

4.1 Support Structure for Printing the Resistors by using a Stripping Method

Building the support structure requires several steps:

Laminating the PCB

First, the solder resist Pyralux PC1025 is applied on the PCB by lamination. A standard laminator unit [Bungard, 2017a] is used. The settings are shown in appendix A. The material is photosensitive and cures under ultraviolet light (UV). To prevent premature curing the process has to take place in a darkroom. The PCB is cleaned with isopropyl and lint-free paper. A copper base board is used to protect the 100 μm thin PCB from deforming. Before applying the solder resist, the base board with the PCB was warmed up with a hot air blower. The PCB is laminated by milling a single layer of solder resist onto it and left to rest for about one day. The protective foil of the solder resist is not removed at this point. It is important to make sure that the solder resist is evenly applied on the PCB, otherwise this layer does not have the same thickness across the whole length of the PCB.

Exposing the PCB to Ultraviolet Light

A mask is used to prevent parts of the solder resist to be exposed to UV light [Scherzer, 2016]. The material used is an ink jet[1] overhead foil. Because the printer can change scaling of the

---

[1]For sufficient opaqueness an ink jet printer is necessary.

mask during printing the file has to be prepared accordingly to prevent misalignment. For
a mask with a pitch of 0.5 mm and a length of 20 cm this is incredibly important. Fig. 4.3
shows the exposure mask. The remaining PCB is covered with light-tight paper.

Figure 4.3: Exposure mask for building the support structure, printed with an ink jet printer.

In the darkroom the exposure mask is aligned and fixed with tape on the PCB. For this, it
was helpful to align the black spots on the exposure mask next to the support structure with
the provided holes in the PCB. As light source a LED without UV-emission is used to align
the exposure mask. During exposure a vacuum of 200 mBar pressure is necessary to prevent
light scattering between the mask and PCB. The PCB is exposed for 90 s. After exposure
the PCB is left to rest for 30 to 60 min. Then the exposure mask and the protective foil of
the solder resist are removed from the PCB. The unexposed solder resist is removed by using
a stripping method leaving only the desired support structure.

Stripping Method

The PCB is submerged in a stripping mixture, consisting of 15 g sodium carbonate (Na_2CO_3)
dissolved in 1 l water. The solder resist is carefully brushed away with a sponge, shown in
Fig. 4.4. It is vital to only keep the PCB submerged for exactly as long as it takes to brush
away the excess solder resist. Keeping it in for too short will not allow the solder resist to be
removed easily, but keeping it in for too long will soften the entire material and possibly result
in damage to the support structure. The best way of dealing with this is stripping the solder
resist only around the support structure first until the copper contacts between the soldering
pads become visible. Then rinse with clear water, blow-dry carefully with compressed air
and finally remove the remaining solder resist from the rest of the PCB. Now it is left to dry
for some hours. Solder resist leftovers from stripping are removed with a scalpel.
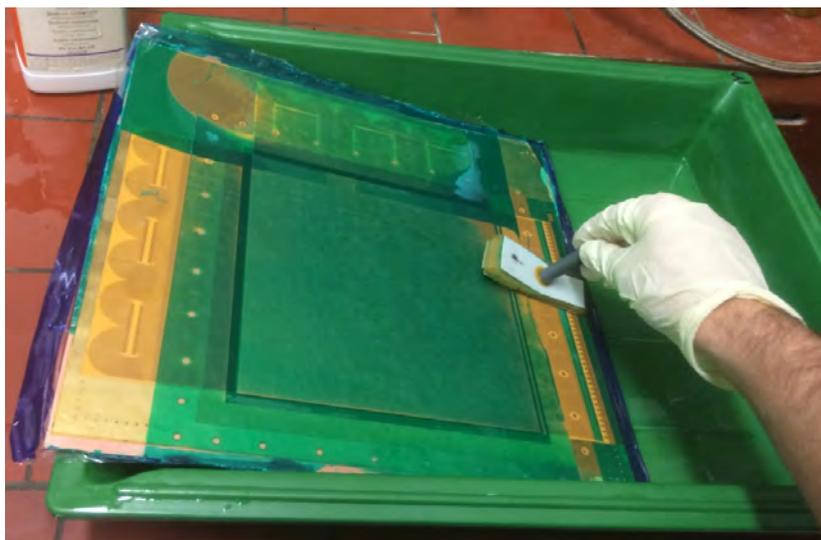

Figure 4.4: Stripping method: The excess solder resist is removed by carefully brushing it
away with a sponge in a stripping mixture, consisting of 15 g Na_2CO_3 dissolved in 1 l water.
Figure taken from [Scherzer, 2016].

4.2 Results of the Stripping Method

The resulting outcome of the support structure is first visible on the dry solder resist. The result is evaluated under a microscope. Fig. 4.5 shows some different results of the stripping method, stars rate the quality of the results. Clearly visible are gaps of different width and different alignment with respect to the anode strips.

The following criteria have to be fulfilled to accept the support structure for the next steps, resulting in the two upmost examples in Fig. 4.5 getting accepted:

- the exposure mask needs to be well aligned with respect to the anode strips

- the solder resist needs to be well attached to the PCB and did not soften or get detached from the PCB

- the gaps need to be opened up well

Figure 4.5: Different results of the stripping method, stars rate the results. In order to accept the support structure the following criteria have to be fulfilled: The exposure mask needs to be well aligned with respect to the anode strips. The solder resist needs to be well attached to the PCB and did not soften nor detached from the PCB. The gaps need to be opened up well. The two examples on top were accepted.

It was observed that gaps closer to the edge opened wider than those towards the center. The process of stripping is least likely the cause of the width differences, because the excess solder resist was carefully brushed away by hand with a sponge, making sure to brush evenly over the entire PCB.

Initially the PCB was laminated horizontally as shown in Fig. 4.6 (left). This can cause the solder resist to be applied unevenly across the entire support structure, for example when the laminating roller stutters during the process. In regions where the laminating roller stops the solder resist is less thick and the gaps can open better while stripping. To prevent a unevenly applied solder resist, it was then laminated vertically as shown in Fig. 4.6 (right), resulting in the solder resist being simultaneously applied across the PCB in the region around the support structure. However, it was observed that the gaps closer to the edge still opened wider than those towards the inside. In consequence the laminating direction it irrelevant to this issue.
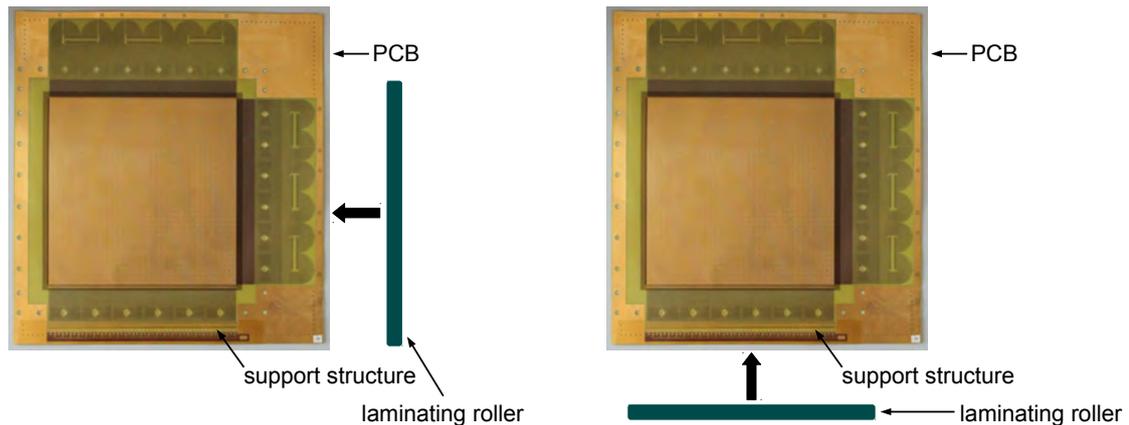

Figure 4.6: Laminating the PCB applying the solder resist from different directions.

A more likely cause of the width differences could be the UV light exposure process. The PCB was placed in the exposure unit as shown in Fig. 4.7. The region around the support structure was located perpendicular to the light tubes. The intensity of UV exposure is higher towards the center due to the Gaussian distributed beam profile of each tube. The solder resist in the center could be hardened more, thus taking longer to open the gaps while stripping.
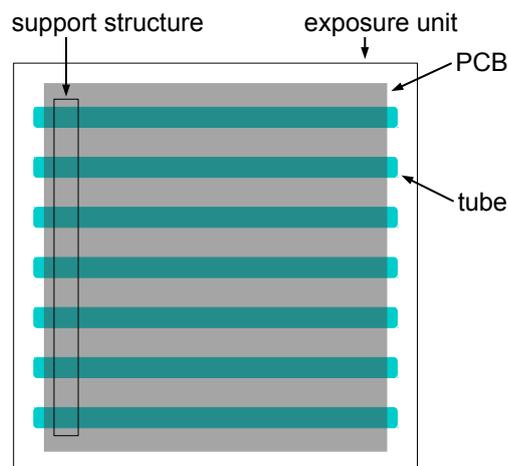

Figure 4.7: When exposing the PCB to UV light it is placed in the exposure unit. The region around the support structure was located perpendicular to the light tubes. Possible differences in UV exposure can cause the solder resist to harden unevenly.

If the resulting support structure is non-satisfactory, the solder resist can be completely removed again before it hardens completely. For this a mixture of $3\,g$ potassium hydroxide (KOH) per $1\,l$ water is used. After some minutes in the mixture the solder resist will be detached from the PCB.

Curing the Solder Resist

Once the support structure is established the solder resist has to harden completely. Otherwise it is still too sensitive and can easily detach from the PCB. The final curing process needs about 2 hours of UV light exposure [Efbe-Schott, 2017], shown in Fig. 4.8. During this time a color change from green to transparent is observed, shown in Fig. 4.9.
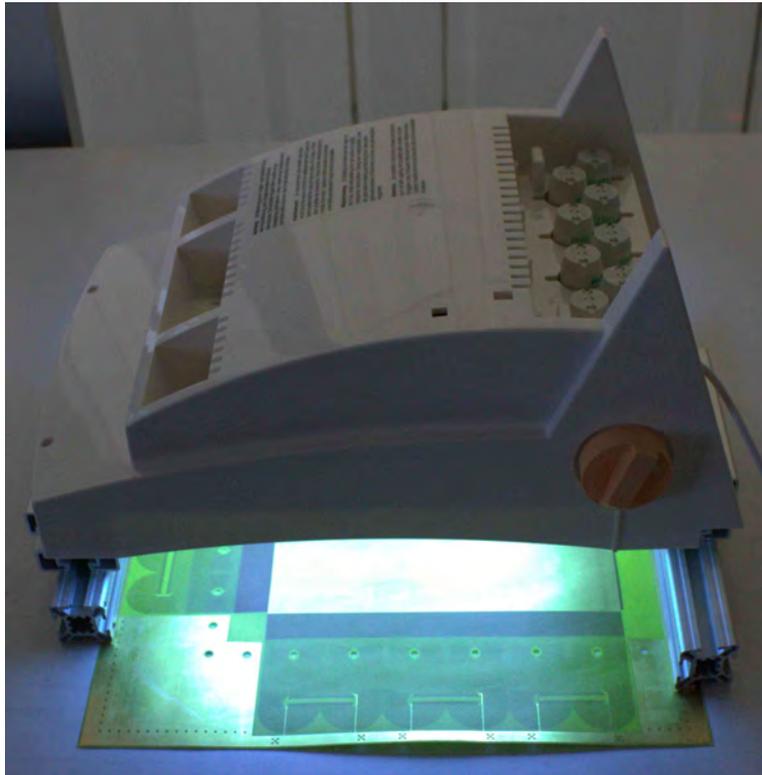

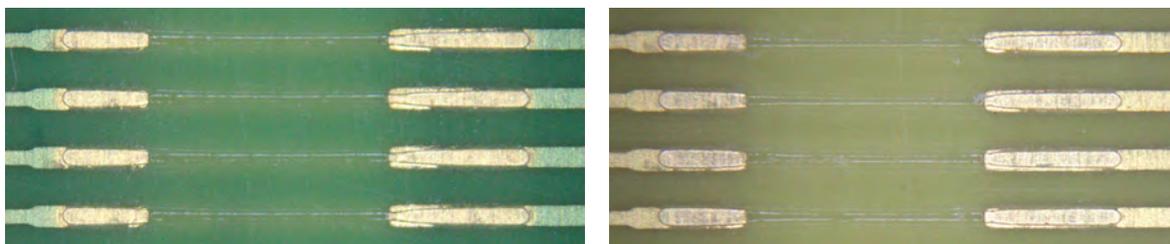Figure 4.8: UV light exposure unit for final curing of the solder resist.

Figure 4.9: During final curing a color change from green (left) to transparent (right) can be observed.

4.3   Printing the Resistors by using a Screen Printing Method

After applying the support structure to the PCB the resistors can be printed. To easily flatten the PCB it gets taped onto a so-called stiffback, shown in Fig. 4.10. This device features a front-plate with holes which enables to generate a vacuum behind this plate, thus molding the PCB into flatness. Mixing different pastes of 100 kΩ/sq and 1 MΩ/sq achieves the desired resistance. A 60 µm thin stainless steel stencil, with 0.2 mm wide gaps and a pitch of the anode strips with 0.5 mm and a squeegee are used, shown in Fig. 4.11, to limit the applied amount of paste on the PCB. The stencil was aligned on the PCB with equal amounts of copper contacts being visible on both ends to prevent the paste from being applied beside to the support structure.
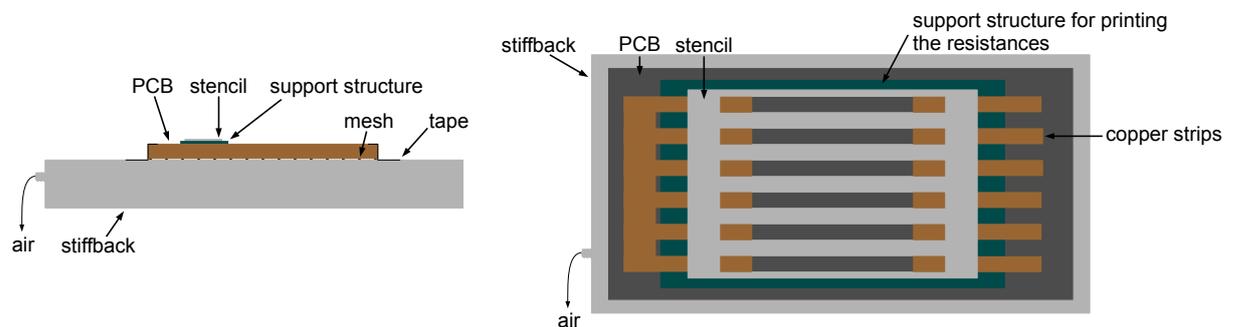

Figure 4.10: Schematic for printing the resistors. To easily flatten the PCB it gets taped onto a so-called stiffback. This device features a front-plate with holes which enables to generate a vacuum behind this plate, thus molding the PCB into flatness. A mesh is used between stiffback and PCB to allow the PCB to be sucked evenly onto the PCB and avoid undesired air locks. A stainless steel stencil is used to limit the applied amount of paste on the PCB.

Figure 4.11: Tools for the screen printing method: stainless steal stencil (bottom) and squeegee (top). The 60 µm thin stencil has three different gap widths where the width of 0.2 mm is used to apply the paste on the PCB.

The paste is spread across all gaps with a stainless steel squeegee, shown in Fig. 4.12 (left). After removing the stencil the paste reaches across the gaps, creating a unified body, see Fig. 4.12 (right). The excess paste is scraped away with the squeegee, see Fig. 4.13 (left) and the excess paste next to the HV contacts is removed with lint-free paper and isopropyl, see Fig. 4.13 (right). In this still liquid form the paste has no conductive properties. Only after fully hardening it for two hours at 150 °C it becomes conductive. The resulting resistors are shown in Fig. 4.14.
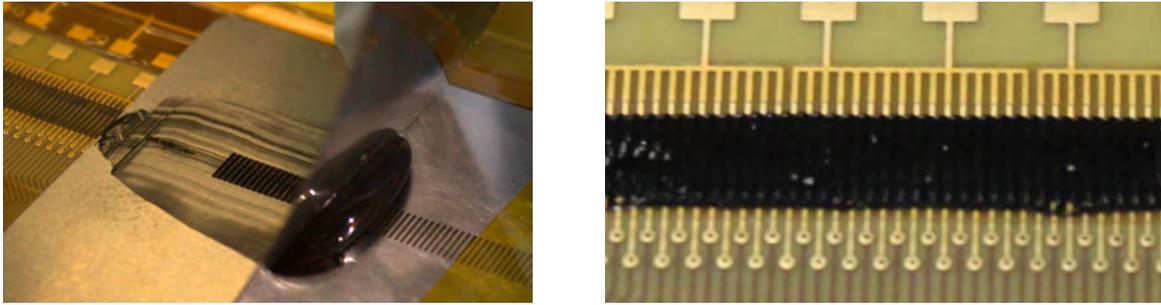

Figure 4.12: Screen printing method: The paste was spread across all gaps with a stainless steel squeegee (left). After removing the stencil the paste reaches across the gaps, creating a unified body (right).
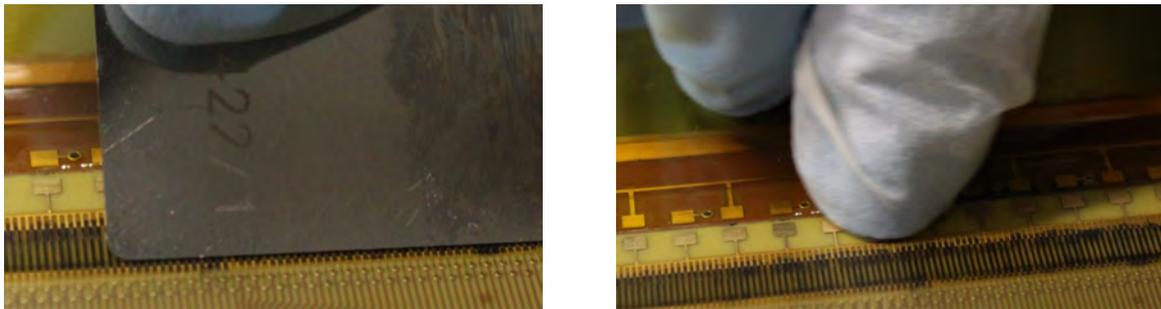

Figure 4.13: Screen printing method: The excess paste was scraped away with the squeegee (left) and the excess paste next to the HV contacts was removed with lint-free paper and isopropyl (right).
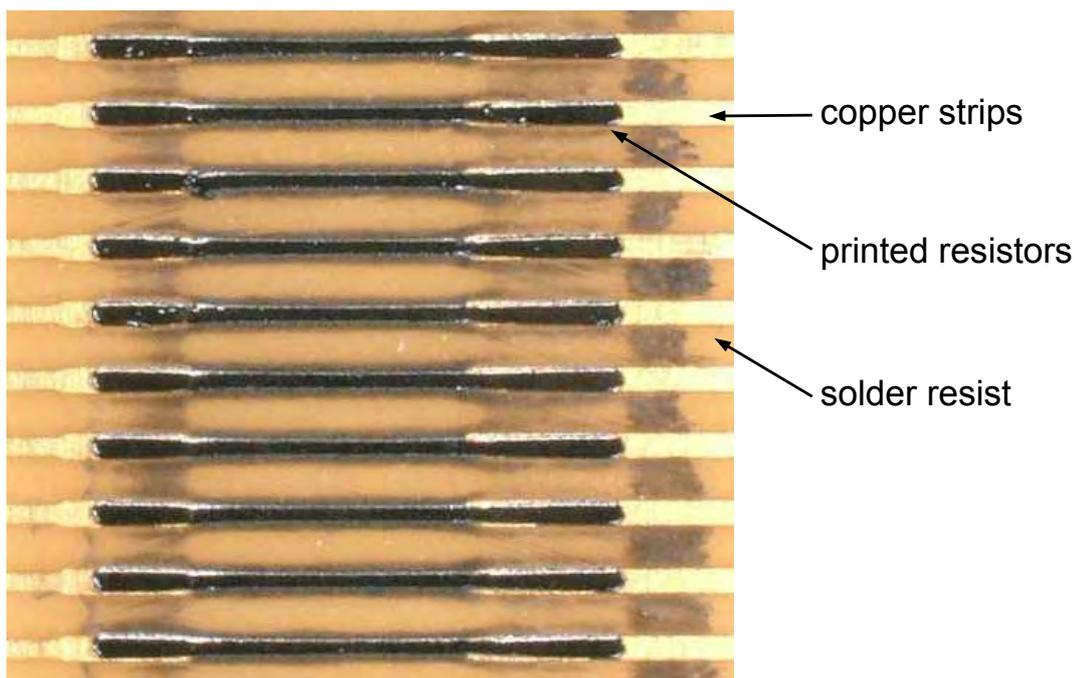
Figure 4.14: Result of the screen printing method: After curing for two hours at $150\,°\mathrm{C}$ the resistive paste becomes conductive.

4.4 Results of the Screen Printing Method

In the following the results of the screen printing method are presented. Furthermore determining the appropriate paste mixture to obtain the desired resistances is explained.

4.4.1 Determining the Appropriate Paste Mixture

The resistance for a straight conductor with constant cross-sectional area A, length l and resistivity ρ can be calculated with

$$R = \rho\,\frac{l}{A}\,. \tag{4.1}$$

The resistance increases with increasing length, but decreases with increasing cross-sectional area. The cross-sectional area A of the resistor can be calculated by the width and the depth of the support structure gap, where the depth correlates with the thickness of the solder resist and and the length l of the resistor correlates with the length of the support structure gap:

$$A = (0.2 \times 0.064)\,\mathrm{mm}^2 \qquad \text{and} \qquad l = 2\,\mathrm{mm}.$$

Different polymer resistive pastes with different resistivity were used, shown in Tab. 4.1. Test prints on several PCBs have been performed to find the appropriate paste mixture with the desired resistance. Since the width of the gaps of the support structure and the resistance before curing could not be measured, the appropriate paste mixture has to be chosen carefully. It was observed that the resistivity of the paste increases as it ages after it has expired past 6 months after the date of approval as stated by the manufacturer.

product no.	lot no.	resistivity [kΩ/sq]	date of approval
RS12116	K743-95	1212.8	04/11/2015
RS12115	K749-2	96.9	04/11/2015
RS12115	K765-92	84.9	10/11/2016

Table 4.1: Available polymer resistive pastes by ESL [ESL, 2017] (see also appendix A, Fig. A.1 to A.3) with different resistivity on a $(5 \times 5)\,\text{mm}^2$ square.

The resistances of each gap connection are measured at $500\,\text{V}$ with a MegOhmMeter by Fluke [Fluke, 2000] to simulate the condition during operation of the detector. Fig. 4.15 shows several test prints on a PCB, starting at the edge (print 1) and ending in the center (print 10), using pure paste RS12115 $_{04/11/2015}$, the mean resistance is plotted against the print. Clearly visible is an increase of the resistance towards the center of the PCB. This is expected due to smaller gap widths and thus less paste in the gaps. Thus the resistance increases, as described in section 4.2.
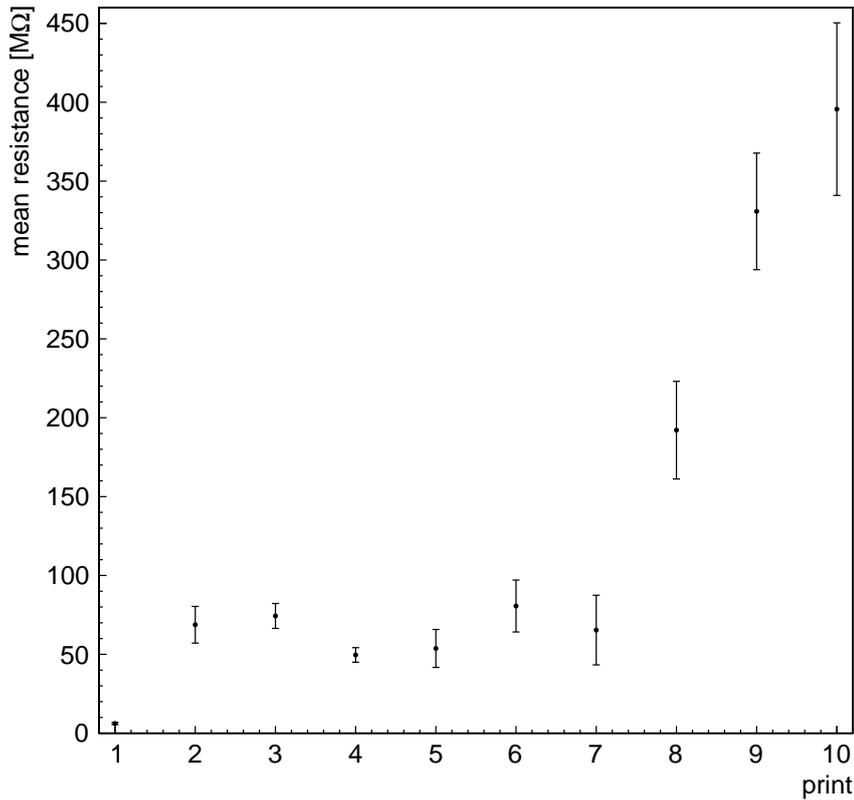

Figure 4.15: Several test prints on a PCB, starting at the edge (print 1) and ending in the center (print 10), using pure paste RS12115 $_{04/11/2015}$ $(100\,\text{k}\Omega/\text{sq})$: The mean resistance is plotted against the print.

Several test prints on a PCB, using different mixtures of pastes RS12115 $_{04/11/2015}$ and RS12116 $_{04/11/2015}$, are shown in Fig. 4.15. The mean resistance is plotted against the paste mixture RS12115 $_{04/11/2015}$: RS12116 $_{04/11/2015}$.
Resistances printed with the same paste mixture lead to the same results, shown in Fig. 4.16 for mixtures RS12115 $_{04/11/2015}$: RS12116 $_{04/11/2015}$ in the ratio 1:0 with a resistance of about $4\,\text{M}\Omega$ and the ratio 9:1 with a resistance of about $30\,\text{M}\Omega$. As expected the resistance increases

when using a higher polymer resistive paste, i.e. a larger quantity of $RS12116_{04/11/2015}$. Due to wider gaps and thus more amount of paste in the gaps for the print with the paste mixture $RS12115_{04/11/2015} : RS12116_{04/11/2015}$ in the ratio 8:2, the resistance is smaller than the resistance with the ratio 9:1.
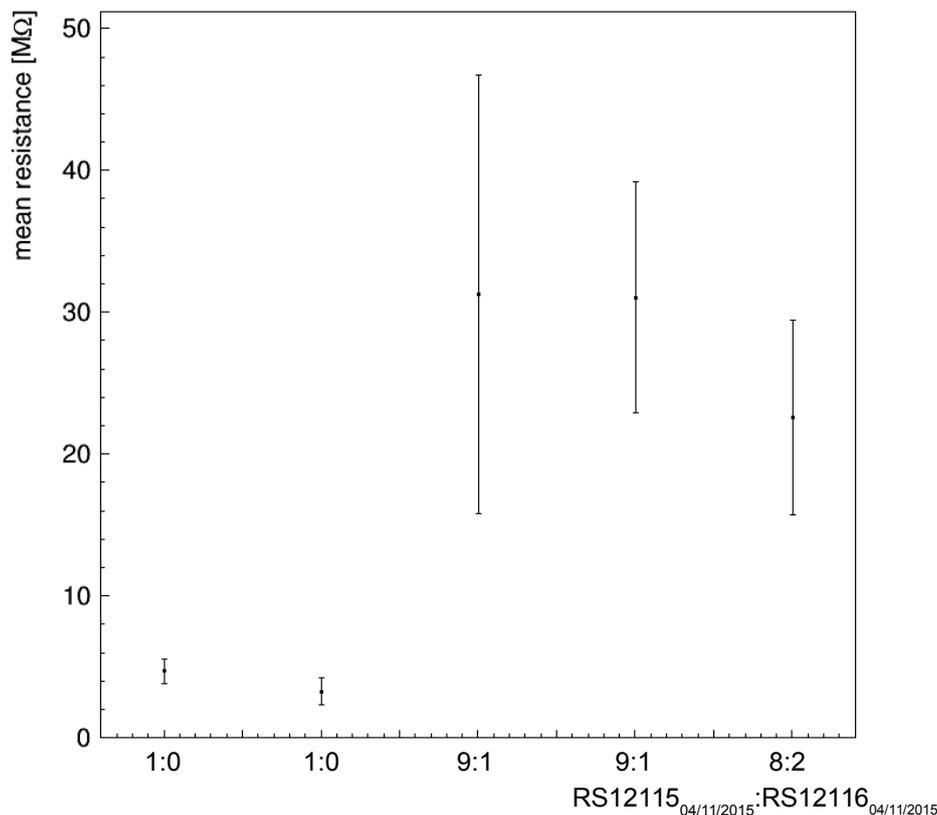

Figure 4.16: Several test prints on a PCB with different mixtures of pastes $RS12115_{04/11/2015}$ ($100\,\mathrm{k\Omega/sq}$) and $RS12116_{04/11/2015}$ ($1000\,\mathrm{k\Omega/sq}$): The mean resistance is plotted against the ratio of the paste mixture $RS12115_{04/11/2015} : RS12116_{04/11/2015}$ (see Tab. 4.1).

Several test prints, using pure paste $RS12115_{04/11/2015}$ on different PCBs, were compared, shown in Fig. 4.17. The mean resistance is plotted against the print. Expected were resistances of the same order. Due to different gap widths and thus different amounts of paste in the gaps the resistances fluctuate.

Furthermore a non-conductive paste RS12MBC by ESL [ESL, 2017] was available. To achieve the target resistance it can be mixed with polymer restive paste. Test prints showed measuring the resistances was not feasible when using this paste, because the resistances were continuously slowly increasing even after 10 min. For this reason it was not used any further.

Since the width of the gaps of the support structure and the resistance before curing could not be measured, the choice of the appropriate paste mixture has to be made carefully.

Various resistances for different gap widths were compared and finally two paste mixtures of $RS12115_{04/11/2015}$ and $RS12115_{10/11/2016}$ were chosen. Since the gap size increases from the center of the PCB towards the edge, different mixtures are necessary to achieve the same amount of resistance in different gaps. One with a ratio of $1:1$ for the inner gaps, one with a ratio of $3:2$ for the outer gaps are chosen.
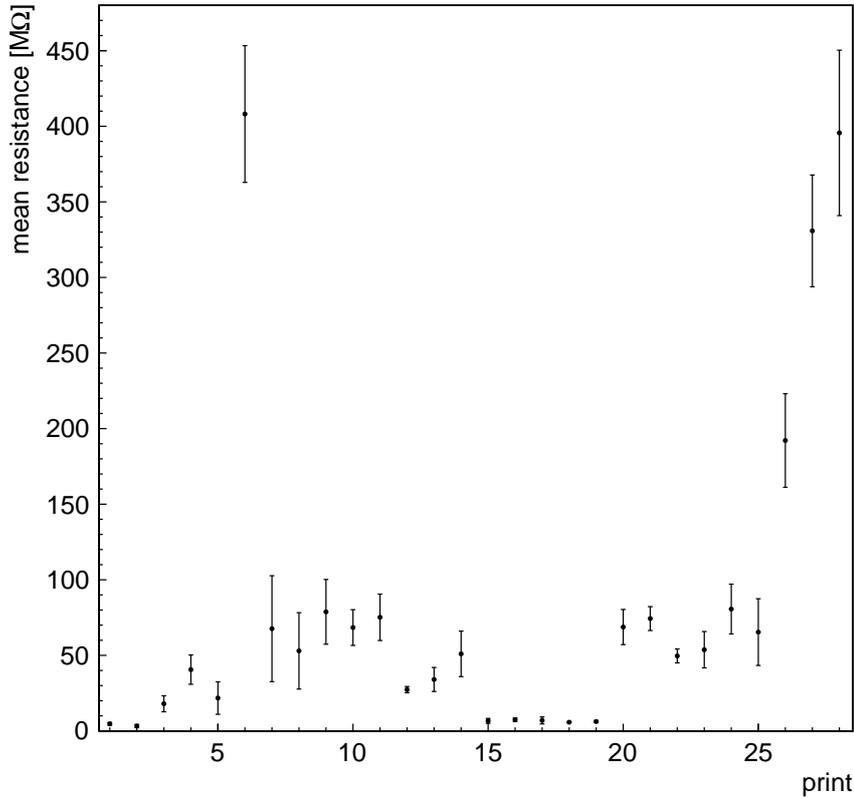
Figure 4.17: Test prints on different PCBs with pure paste RS12115 $_{04/11/2015}$ ($100\,\mathrm{k\Omega/sq}$):
The mean resistance is plotted against the print. Due to different gap widths and thus
different amounts of paste in the gaps the resistances fluctuate.

4.4.2 Resistances

The resistances of each gap connection are measured at $500\,\mathrm{V}$ with a MegOhmMeter by Fluke
[Fluke, 2000] to simulate the condition during operation of the detector. A sample of 234
resistances were measured individually over the entire anode and are shown in Fig. 4.18, filled
in a histogram. The mean resistance can be extracted by a Gaussian fit to the upper part of
the distribution, resulting in a mean resistance of $R = (11.95 \pm 3.22)\,\mathrm{M\Omega}$, which is of a factor
of 0.6 smaller than the desired resistance of about $20\,\mathrm{M\Omega}$.

For verifying that the anode strips are individually connected to the HV contact, the resistors
are tested for interconnection. First the groups, consisting of 16 resistors, see Fig. 4.1 (right),
and afterwards single resistors were tested. For series and parallel circuits applies Ohm's law:

$$R_{\mathrm{series}} = \sum_i R_i \qquad \text{and} \qquad \frac{1}{R_{\mathrm{parallel}}} = \sum_i \frac{1}{R_i}. \qquad (4.2)$$

The interconnection of individual resistors has to be tested by measuring at non-neighboring
contacts, because neighboring resistors are too close to each other that applying high voltage
for measuring results in a spark between the contacts. This damages the PCB.
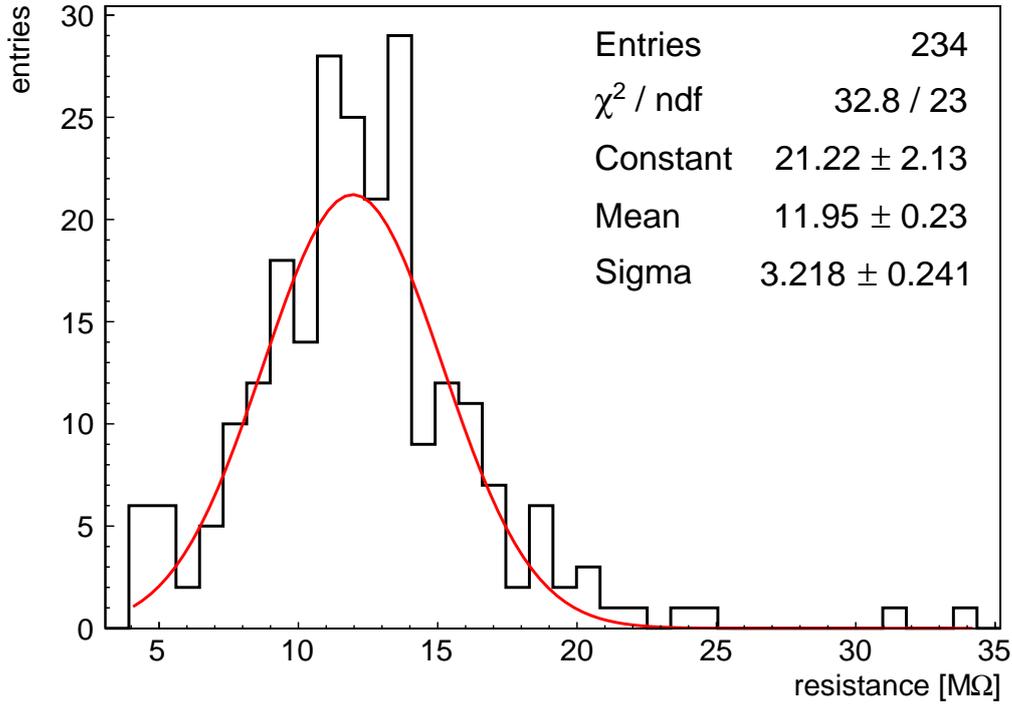
Figure 4.18: Printed resistors on the anode: distribution of a sample of 234 from 384 resistances, measured individually over the entire anode. To simulate condition during operation of the detector they were measured at 500 V.

First two resistors R_1 and R_2 are measured individually, shown in Fig. 4.19 (left). Afterwards they are tested for interconnection. If the measured resistance R_{total} is the sum of R_1 and R_2, corresponding to a series circuit, shown in Fig. 4.19 (right), R_1 and R_2 are series-connected, meaning they are not short-circuited.

The total resistance R_{total} of the circuits in Fig. 4.19 can be calculated by

$$
\begin{aligned}
\text{left}: \quad \text{top:} \quad & R_{\text{total}} = R_1 \\
\text{bottom:} \quad & R_{\text{total}} = R_2 \\
\\
\text{right}: \quad & R_{\text{total}} = R_1 + R_2 \,.
\end{aligned}
\tag{4.3}
$$

If the measured resistance is obviously smaller than the smallest resistance, it can be assumed that they are interconnected, because R_{total} of a parallel circuit is smaller than the smallest resistance in that circuit. An example for interconnection is shown in Fig. 4.20.
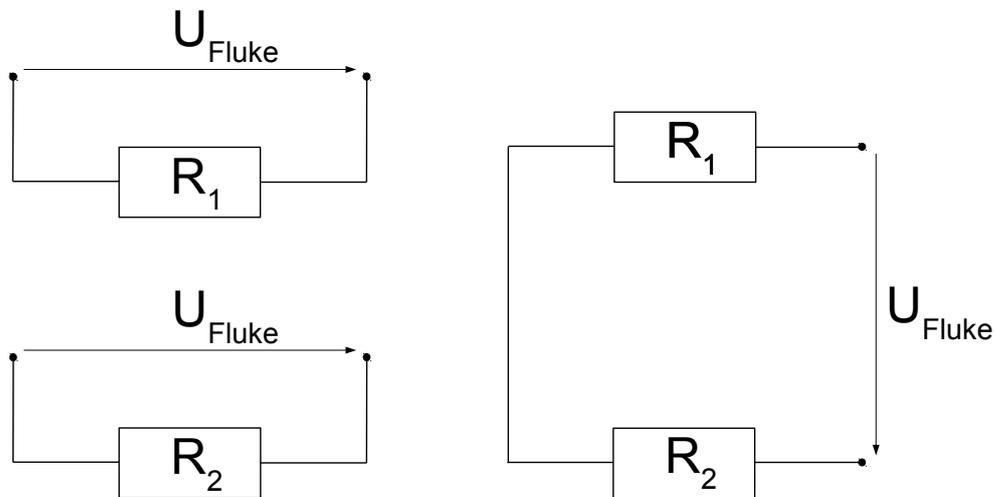
Figure 4.19: Test for possible interconnection of two non-neighboring resistors: First, the resistors R_1 and R_2 are measured individually (left). In case of no interconnection with neighboring resistors, both resistors are series-connected (right). The calculation of the total resistance R_{total} of the circuits is shown in eq. 4.3.
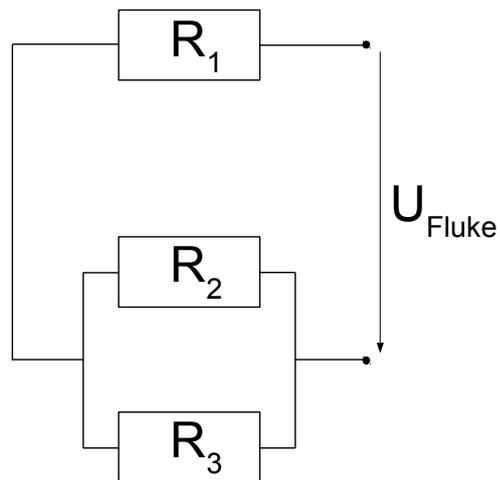

Figure 4.20: Example for a possible interconnection of two non-neighboring resistors: In case R_2 is interconnected with its neighbor R_3, R_2 and R_3 are parallel-connected, with R_1 series-connected. The calculation of the total resistance R_{total} of the circuit is shown in eq. 4.4.

The total resistance R_{total} of the circuit in Fig. 4.20 can be calculated with

$$R_{\text{total}} = R_1 + R_{23} = R_1 + \frac{R_2 \cdot R_3}{R_2 + R_3} \,. \tag{4.4}$$

Similarly the interconnection of the resistors can be verified without individually measuring the resistances first. By using the sample with $R = (11.95 \pm 3.22)\,\text{M}\Omega$ the total resistance can be calculated with

$$\text{no interconnection}: \ R_{\text{total}} = 2\,R \qquad \longrightarrow \qquad R_{\text{total}} = 23.90\,\text{M}\Omega$$

$$\text{interconnection}: \quad R_{\text{total}} = \frac{3}{2}\,R \qquad \longrightarrow \qquad R_{\text{total}} = 17.93\,\text{M}\Omega\,.$$

The difference ΔR_{total} of both circuits can be determined with $\Delta R_{\text{total}} = R_{\text{total,no int}} - R_{\text{total,int}} = 5.97\,\text{M}\Omega$ and is therefore larger than the $RMS = 3.22\,\text{M}\Omega$ of the resistance distribution in Fig. 4.18.

Possible short-circuits between resistors could be eliminated by scraping off the resistive paste carefully with a scalpel under the microscope. Normally this is not necessary. Finally it can be stated that the anode strips are individually connected to HV.

Furthermore the alignment of the support structure gaps to the anode strips affects the resistances. As it can be seen in Fig. 4.21, due to poor alignment the length of the front edge between resistor and anode strip (yellow and red) decreases. Electrons at the side edge (green) travel a longer distance through the resistor than electrons at the front edge (red) and thus the resistance increases.
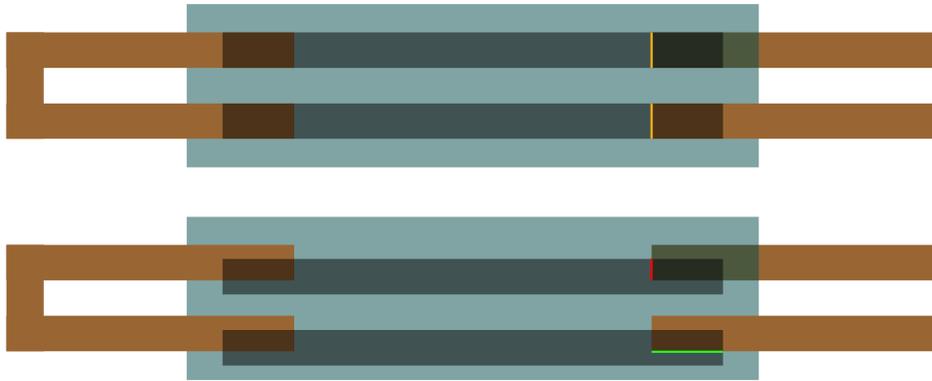

Figure 4.21: Good alignment (top) and poor alignment (bottom) of the support structure gaps to the anode strips. Due to poor alignment the length of the front edge between resistor and anode strip (yellow and red) decreases. Electrons at the side edge (green) travel a longer distance through the resistor than electrons at the front edge (red) and thus the resistance increases.

It is furthermore observed that the resistances decrease with repeated baking, which corresponds to the observations of [Klitzner, 2016b], where a reduction of the resistances of about 10 % for an additional baking process is observed. Fig. 4.22 shows how the resistances change each time. The fraction of resistance, where 1 corresponds to the resistance after the first baking of two hours, is plotted against the curing time while baking. This behavior allows reducing the resistance after the specified curing time of two hours, if it is too large. This is not desirable, of course, since the PCB is very sensitive and should only be heated for as short as possible.
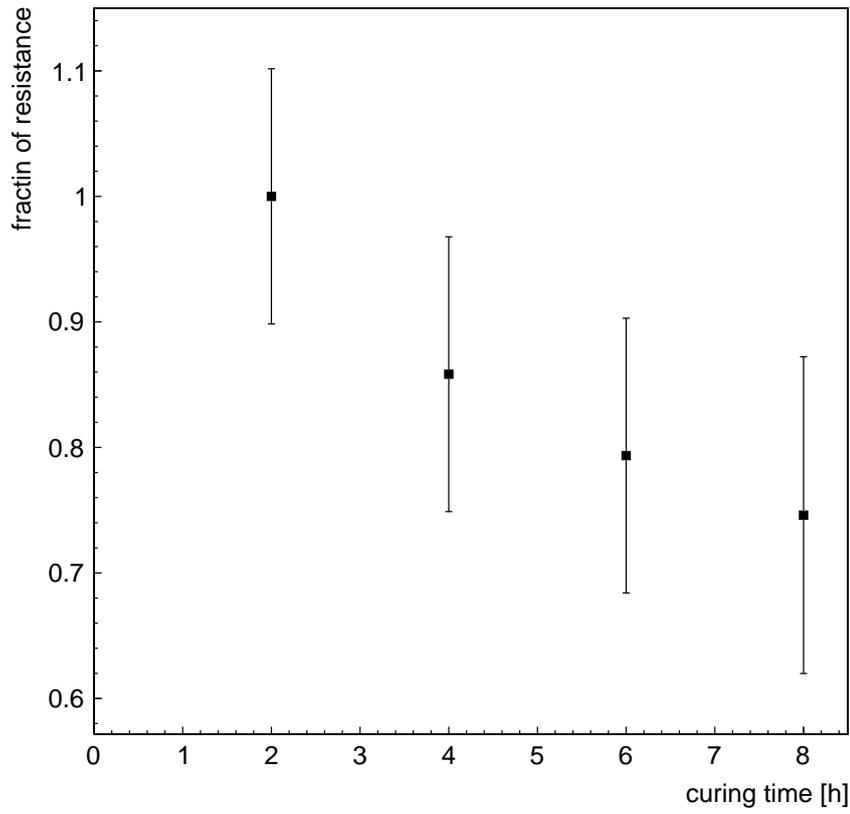
Figure 4.22: The resistances decrease with additional baking processes. The fraction of resistance, where 1 corresponds to the resistance after the first baking of two hours, is plotted against the curing time while baking.

4.4.3   Improving the Screen Printing Method

First a rough mesh with a 250 µm wire diameter and a wire pitch of about 1.5 mm was used between stiffback and PCB to allow the PCB to be sucked evenly onto the PCB and avoid undesired air locks. A print where this mesh was used is shown in Fig. 4.23. Observed were periodically occurring paste residues (dark spots), which could not be removed by scraping with the squeegee, whereby several resistors are connected to each other. Using a significantly finer mesh with a 90 µm wire diameter and a wire pitch of about 0.3 mm did not leave any paste residues on the solder resist. Due to the rough mesh the PCB is not completely flat when sucked onto the stiffback.
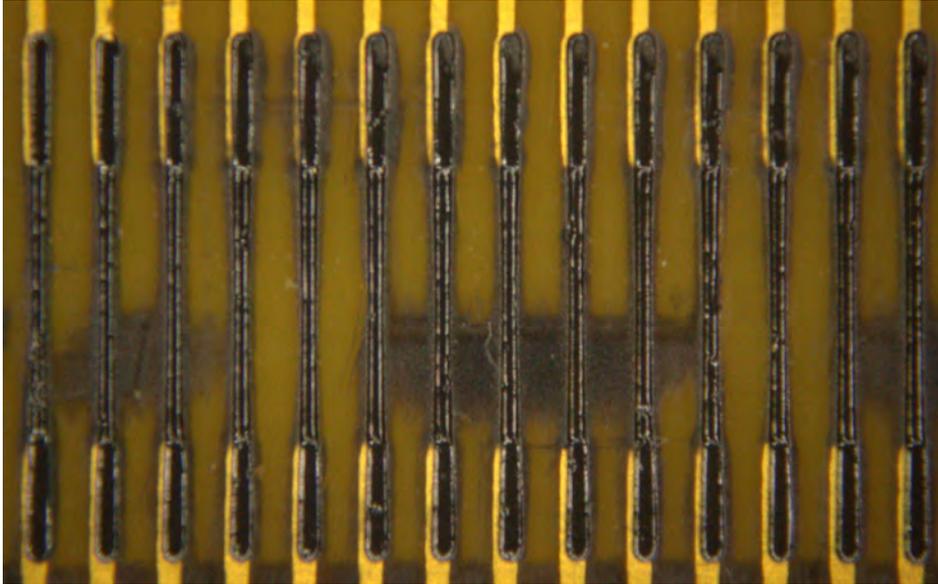
Figure 4.23: Printing the resistors by using a rough mesh with a 250 µm wire diameter and 1.5 mm wire pitch between stiffback and PCB to allow the PCB to be sucked evenly onto the PCB and avoid undesired air locks. Visible are periodically occurring paste residues, which could not be removed by scraping with the squeegee, whereby several resistors are connected to each other.

Furthermore in Fig. 4.24 a result of the screen printing method can be seen, where the solder resist softened while stripping. The solder resist got detached from the PCB, visible in Fig. 4.24 (right), and became wavy where the paste could not be removed by scraping with the squeegee and interconnected the resistors.
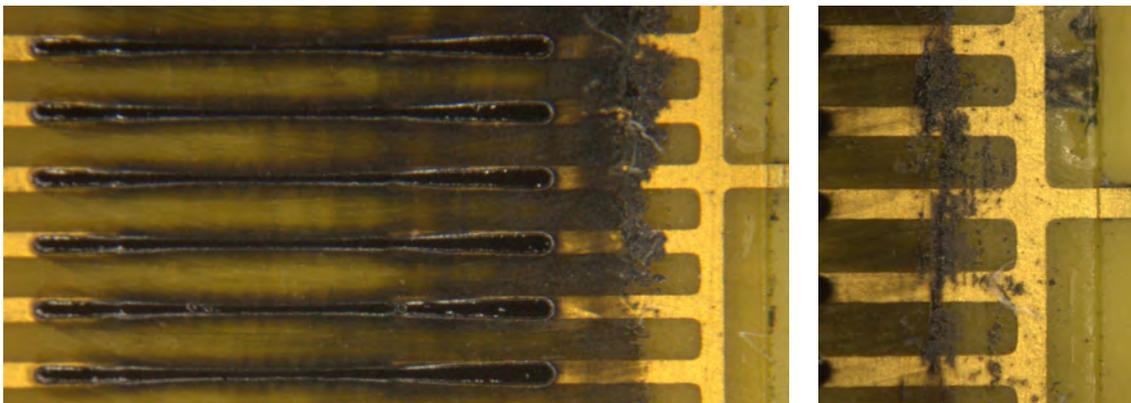

Figure 4.24: Result of the screen printing method: Due to softening the solder resist detached from the PCB and became wavy. The paste could not be removed by scraping with the squeegee as desired (left). A close-up of the detachment is shown on the right.

4.5   Summary and Outlook

The resistors connecting the anode strips individually to HV are printed with an optimized screen printing method. To obtain suitable resistances for all anode strips, a good quality support structure made out of solder resist with constant gap width is required.

Desired resistances can be obtained with a suitable paste, even if the gaps are not wide open. It is necessary that the gaps are evenly wide, otherwise different amounts of paste distributed into the gaps will cause uneven resistances on individual strips. Alternatively the resistors would have to be printed individually with different paste mixtures, which would be as time consuming as soldering resistors.

The stripping method to build the support structure works perfect on the used, thicker test PCBs. On thin PCBs the gaps do not always open evenly. Only after drying the solder resist the results of the stripping method can be observed under the microscope.

If the resulting support structure is non-satisfactory, the solder resist can be completely removed in a mixture of $3\,g$ potassium hydroxide (KOH) per $1\,l$ water. After some minutes in the mixture the solder resist will be detached from the PCB. Subsequently, a new support structure can be repeatedly built, until the result is satisfactory. Removing the solder resist and rebuilding a support structure can damage the PCB. By often touching the PCB, deformation and damage can occur.

To ensure best results for each process, the stripping method can be further optimized as described next.

Optimising the Stripping Method

During the stripping process the solder resist softens fast and eventually detaches from the PCB. Meanwhile the gaps of the support structure might not open evenly or at all. Two ways were found to make the solder resist more resistant. Increasing the exposure time between laminating and stripping allows the solder resist to cure more and get attached better to the PCB. Increasing the rest time between exposure and stripping lets the solder resist harden more. In both cases it does not soften as fast when stripping, providing more time for the gaps to open. In order to find a suitable mix of exposure time and rest time, more tests have to be made.

The aligned and attached exposure mask has to be sucked onto the PCB during exposure to prevent scattering light. With the available exposure unit only an exposure from below was possible, because the light tubes are located on the bottom. As a result the PCB and the attached mask had to be flipped before exposure. This could cause the mask to slip out of position, resulting in a non-perfect alignment during exposure.

Ideally an exposure unit is used which allows the mask to be attached after the PCB has been placed inside. The PCB can then be exposed without touching it again between alignment and exposure.

Extending the PCB Layout

Increasing the pitch of the anode strips and thus the layout of the support structure would possibly allow the gaps to open better and more evenly. This can be achieved by extending the layout of the PCB around the HV contact of the anode strips. More solder resist material would end up between the gaps, meaning the solder resist would not soften as fast and detach from the PCB. This would possibly give more time to strip the PCB and open the gaps.

If not all gaps of the support structure are properly opened up and equally wide, they will contain a different amount of paste and thus the resistances are not at the same value.

Chapter 5

Assembly and Initial Studies of a Thin Two-Dimensional Floating Strip Micromegas Detector

The following chapter deals with the assembly of a thin floating strip Micromegas detector with a two-dimensional readout structure. The functional principle of a floating strip Micromegas detector was introduced in section 3.1. Work steps for the production of single detector parts, especially the optimization of the thin anode, and the assembly of the detector are described in this chapter. After assembly of the detector initial studies have been carried out.

5.1 Optimization of the Anode

The anode is a PCB made out of Kapton with photo-lithographically produced anode strips with a pitch of 0.5 mm and a width of 0.3 mm. The number of anode strips is increased from 128 to 384 strips [Scherzer, 2016]. This results in a (19.2 x 19.2) cm^2 active area.

5.1.1 Pillars

A pattern of 150 µm high pillars is needed to hold the micro-mesh at a constant distance to the anode. This allows to obtain a constant amplification region between anode and mesh. The pillars are arranged in a grid of 38 x 38 pillars with a pitch of 5 mm, a schematic is shown in Fig. 5.1 (left). They are made of a 75 µm thick solder resist by Bungard [Bungard, 2017b] and created with the stripping method, consisting of the same steps as making the support structure (see chapter 4), shown in Fig. 5.1 (right). However, two layers of solder resist are necessary to get a pillar height of 150 µm. A frame, on which the mesh rests, defines the active area of the detector. This is built together with the pillars. The PCB is laminated again with a single layer of solder resist, making sure that the area around the support structure is not laminated. After letting the laminated PCB cool for about 15 min, the protective foil of the solder resist was removed and the PCB was laminated with the second layer. The exposure mask, shown in Fig. 5.2, was aligned and fixed on the PCB. After the exposure the PCB was cleared of excess material, making sure that the area around the support structure was not put into the stripping mixture, consisting of 15 g Na$_2$CO$_3$ dissolved in 1 l water. The remaining material is finally cured under an exposure unit. After building the support structure, frame, on which the mesh rests, and pillars the resistors can be printed.
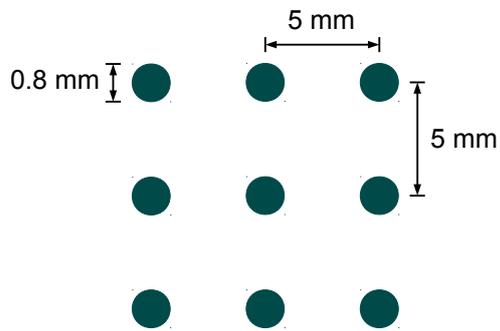
Figure 5.1: Pillar-shaped spacer structure in the active area on the surface of the anode to hold the micro-mesh at a constant distance of 150 µm to the anode. They are made of solder resist, created with the stripping method and arranged in a raster of 38 x 38 pillars. 2% of the active area is covered with pillars (left). A photograph of a pillar with a diameter of 0.8 mm taken under the microscope (right).
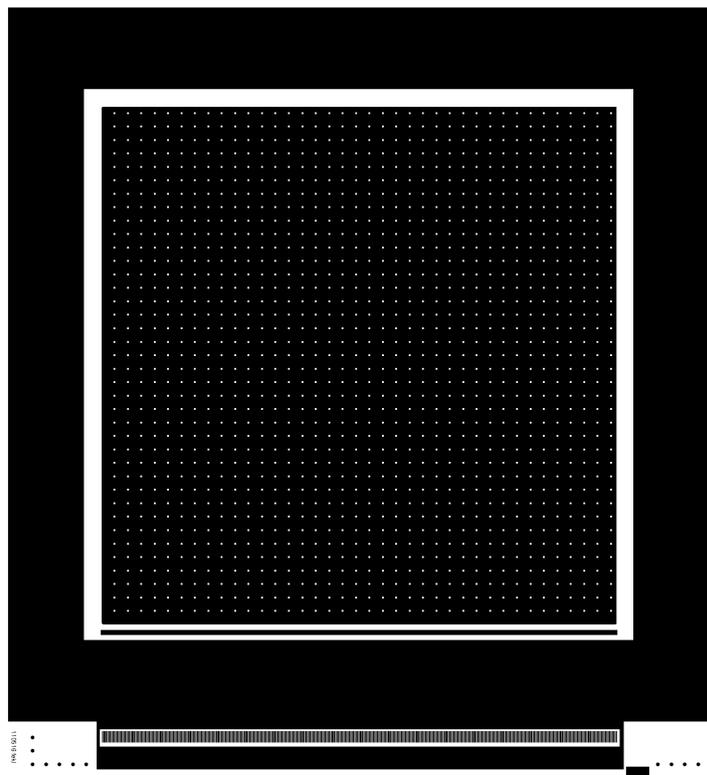

Figure 5.2: Exposure mask for the stripping method. The support structure for printing the resistors can be seen on the bottom, mesh frame and pillars made of solder resist were built to hold the micro-mesh at a constant distance to the anode.

5.1.2 Improving the Soldering Process of the Panasonic Connectors

Reading the detector output requires the anode to be connected to the APVs. For this AXK5SA3277 Panasonic connectors with 130 pins [Panasonic, 2017] are soldered on the back-side of the PCB. Each connector can read 128 strips. Six connectors are used to get both x and y data from 384 strips. A method for soldering the connectors to the thin anode was developed. The setup is displayed in Fig. 5.3.
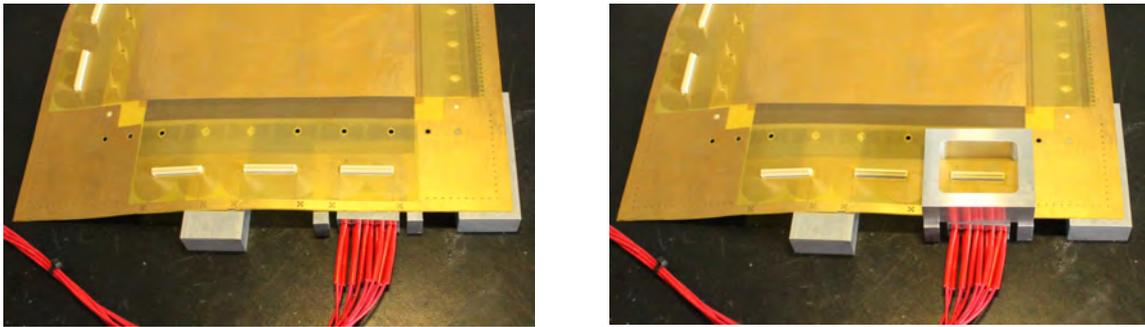

Figure 5.3: Soldering the Panasonic connectors: Afterwards the PCB is put on the brass block. The Panasonic connectors were placed on the soldering paste (left). To flatten the PCB while soldering an aluminum frame was put onto the PCB around the connector (right).

Soldering was done with a mechanic soldering paste WG-50 with Sn : Pb 63 : 37 weight-% alloy, which is commonly used by the industry for machine soldering stations. To apply it on the desired locations a stencil is aligned with the PCB. Using a squeegee the paste is applied through the stencil. Afterwards the PCB is put on a $(40 \times 20 \times 20)\,\text{mm}^3$ brass block, plugged with five heating elements made for a 3D printer, shown in Fig. 5.4, operated with 20 V. With tweezers the Panasonic connectors were placed on the paste and weighed down to flatten the PCB and ensure contact between anode and connector and prevent it from moving, as the paste liquefies under heat. When the soldering paste is liquid it turns from grey to silver and transforms into solder. After around 60 to 80 s and at a temperature of about 180 °C, when the color-change becomes visible on both sides of the connector, the PCB has to be removed from the block immediately to prevent damage of the thin anode. After cooling, the result is reviewed under the microscope. The pins are individually checked whether they were soldered and any short circuits where fixed with a pointed soldering iron.
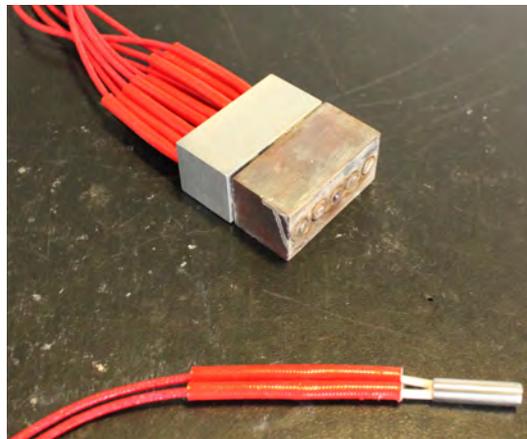

Figure 5.4: Brass block plugged with five heating elements (top) and a single heating element (bottom).
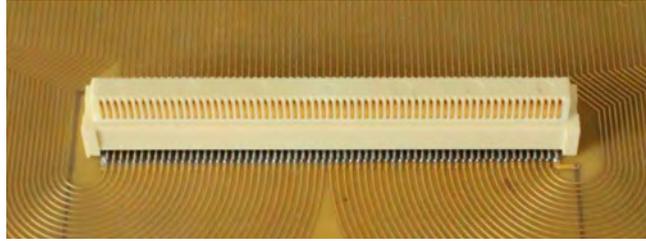
Figure 5.5: Soldered Panasonic connector on the PCB.

5.1.3   Paper Honeycomb Support Structure

To stabilize the 100 µm thin PCB a PVC frame is glued onto the backside. For this the PCB has to be attached to the stiffback (see section 4.3) at a constant pressure of 950 mbar, but with the pillars facing the stiffback. Height differences caused by the various elements attached to the top would lead to deformation. To compensate for this, tape with a thickness of 150 µm is applied around the active area. Furthermore all holes like vias and screw holes are masked with Kapton tape, to prevent glue from getting sucked in. For gluing a two-component adhesive by [UHU, 2017] based on epoxy resin with a curing time of 12 hours and a processing time of 60 min is used. First, the glue is applied on the PVC frame by using a gluing tool with a 0.3 mm notch. Second, the glue is prepared with a filler comb. This procedure allows the glue to balance out minor irregularities on the surface of the PVC frame. Then the frame is pressed against the PCB and weighted with lead. Another frame, made of aluminum-profiles, is positioned around the PVC frame to hinder it from floating out of position on the glue.

An 8 mm thick commercial grade aramid fiber paper honeycomb is glued onto the backside of the anode, in the active area of the detector inside the PCV frame. Glue is applied as thinly as possible on the PCB, but still covering the entire active area. The other side of the honeycomb is plastered with a 10 µm thick aluminum vaporised Kapton foil beforehand. This prevents bending of the thin anode during detector operation due to gravitational sag of the honeycomb and anode.
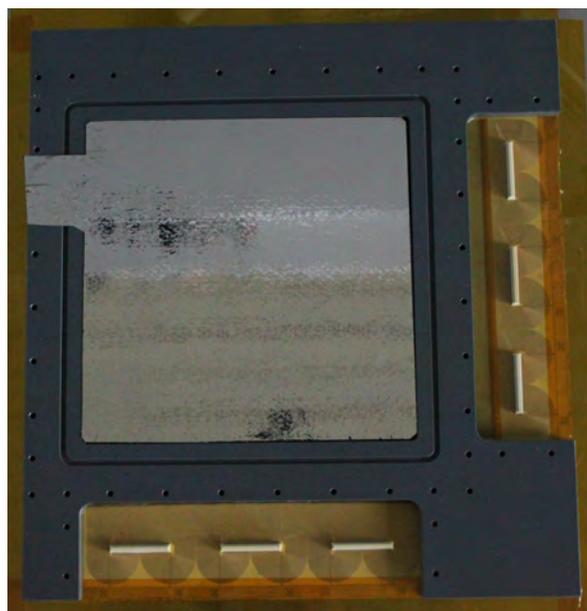

Figure 5.6: Anode with glued PVC frame and paper honeycomb inside the PVC frame, plastered with a 10 µm thick aluminum vaporised Kapton foil beforehand.

After the gluing process has finished, glue residues which were sucked into screw holes had to be removed.

Finally $1\,k\Omega$ SMD resistors are soldered onto the group contacts of the anode strips and the HV cable is soldered to the anode. Since the anode is only $100\,\mu m$ thin, it is necessary to work very carefully and quickly in soldering so that the Kapton layer between the HV contacts on the top of the anode and the grounded copper layer on the underside was not damaged by the heat of the soldering.

5.1.4 Topology of the Anode

In order to make statements about the planarity of the anode and visualize possible deformations in the active area of the detector, the topology of the anode was measured with a coordinate measuring machine (CMM). Deformations in the active area can limit the functionality of the detector due to different gains in the amplification region. For this the finished anode was placed on a near-perfect planar granite table. The CMM scans the surface of the anode point by point in two dimensions. At each position the distance to the surface of the anode is measured with a blue laser by Micro-Epsilon [Mirco-Epsilon, 2017] at an angle of 13.8°, described in detail by [Müller, 2017]. In this way one obtains the topology of the anode, as shown in Fig. 5.7. The measurement consists of 500 x 500 measured points with a distance of 0.52 mm between each measured point.
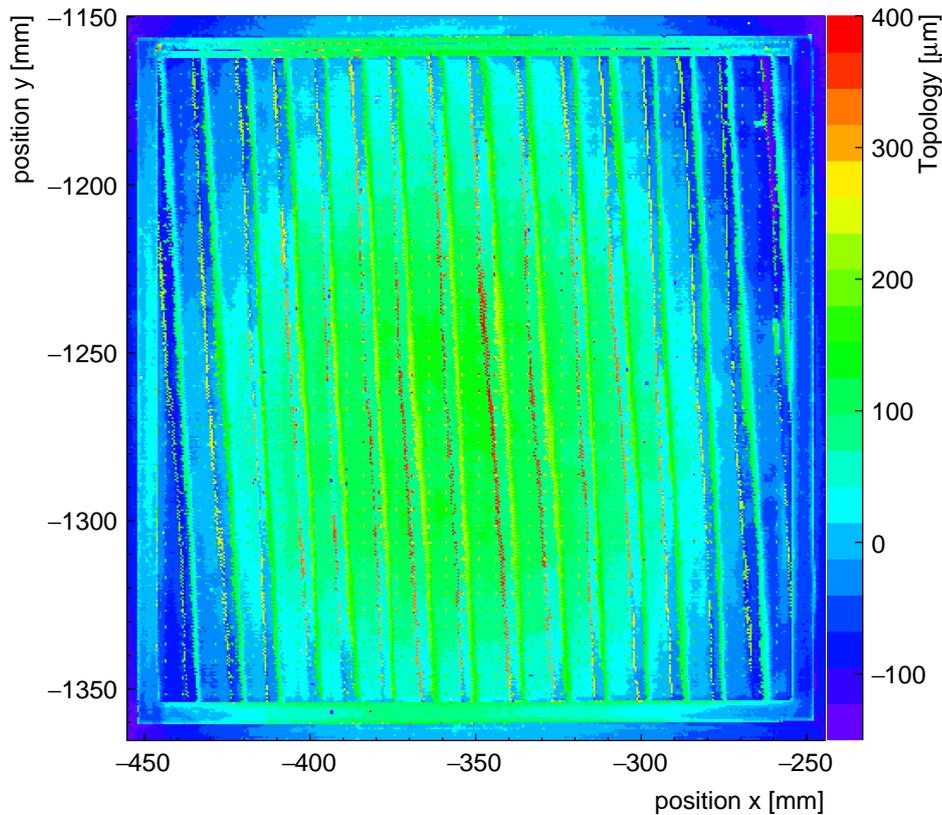

Figure 5.7: Topology of the anode in the active area of the detector, measured with the CMM on a planar granite table. First, a reference measurement of the granite table was subtracted from the measurement to obtain the topology of the anode.

The active area of the detector is clearly visible, surrounded by the frame out of solder resist, as well as the pillars, arranged in a raster, distributed over the active area. Furthermore, periodic strip patterns over the entire active area are visible. After examining the PCB again, possible deformations due to the periodic strip pattern were excluded. A possible explanation is an interference pattern caused by the pitch of the anode strips and the measured points.

Therefore a more precise measurement over a $(5 \times 5)\,\text{cm}^2$ space of active area with a measuring point distance of $0.1\,\text{mm}$ was made to prevent the interference pattern. Fig. 5.8 shows the precise measurement. No periodic strip pattern is visible, which suggests that it has to be an interference pattern. Clearly visible are the pillar structure with height of around $150\,\mu\text{m}$ as well as the anode strips. Small local deformations of several micrometers are also visible.
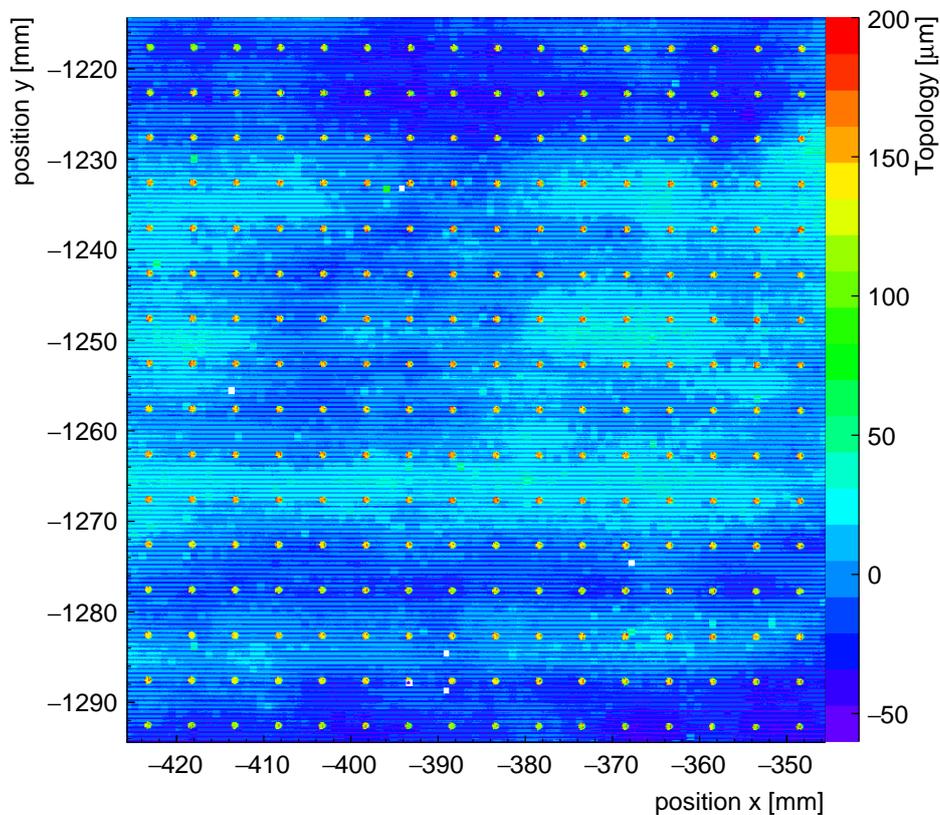

Figure 5.8: Topology of a section of the anode in the active area of the detector, measured with the CMM on a planar granite table. The reference measurement of the granite table was subtracted from the measurement.

A precise measurement over the entire active area of the detector without interference pattern obtaining a measuring point distance of $0.1\,\text{mm}$ would take around 28 days and was therefore not possible. In order to visualize possible deformations over the desired active area it was attempted to filter out the interference pattern by using a Fourier transformation.

Fourier Transformation

A Fourier transformation allows continuous, periodic signals to be transformed into a discrete frequency spectrum. Fig. 5.9 (left) shows a desired measurement in x direction for a position in y direction. Clearly visible is the periodic pillar structure. The goal was first to show that

the periodic pillar structure, shown in Fig. 5.9 (right), can be filtered out with the Fourier transformation. Both projections in Fig. 5.9 were Fourier transformed. The difference in real and imaginary part of the result was calculated to obtain the real and imaginary part of the Fourier transformed topology of the anode surface without pillar structure. Fig. 5.10 shows the projection in x of the topology of the anode with pillar structure (black), see also Fig. 5.9 (left), and the backward Fourier transformed topology (red). Remaining is the topology of the anode without the pillar structure. It was possible to filter out the periodic structure of the pillars.
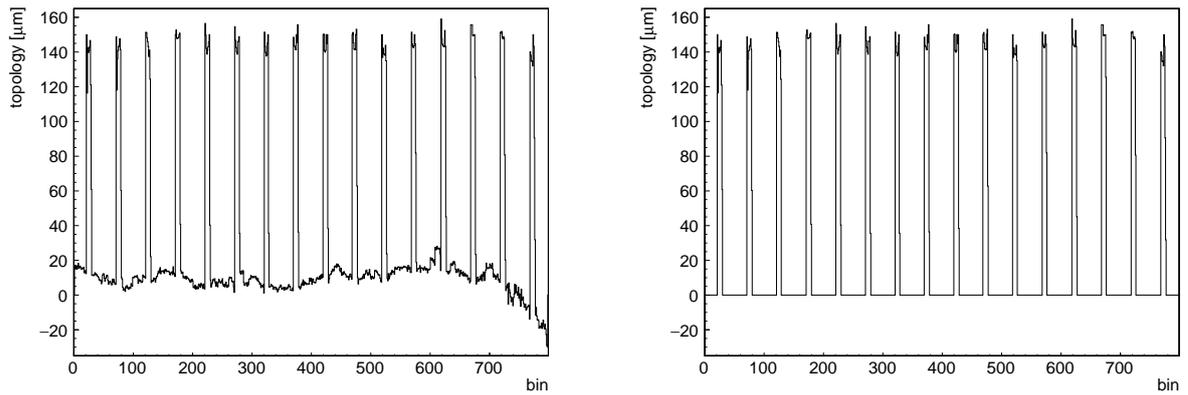

Figure 5.9: Topology of the anode: total projection in x (left) and the pillar structure of the projection in x (right).
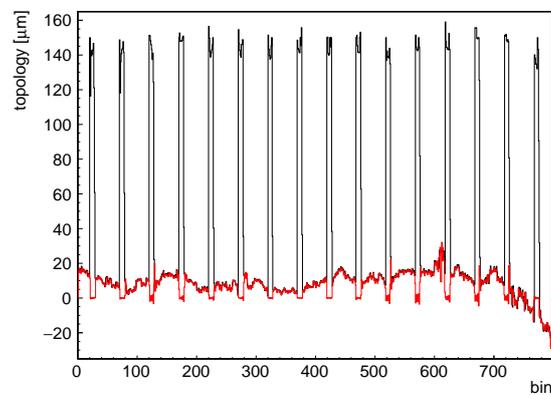

Figure 5.10: Topology of the anode: projection in x (black), backward Fourier transformation resulting in the topology of the anode without pillar structure (red).

Determining the Topology of the Anode

Sharp periodic patterns have broad spectra in the Fourier transformation. Due to a superposition of the frequencies of the interference patterns in the measurement over the active area it was not possible to filter them out, because it was not possible to assign these frequencies.

In Fig. 5.11 the distribution of the topology from Fig. 5.7 can be seen, plotted in a histogram. Visible are three peaks. The first peak at about -100 μm relates to the area outside the active area.
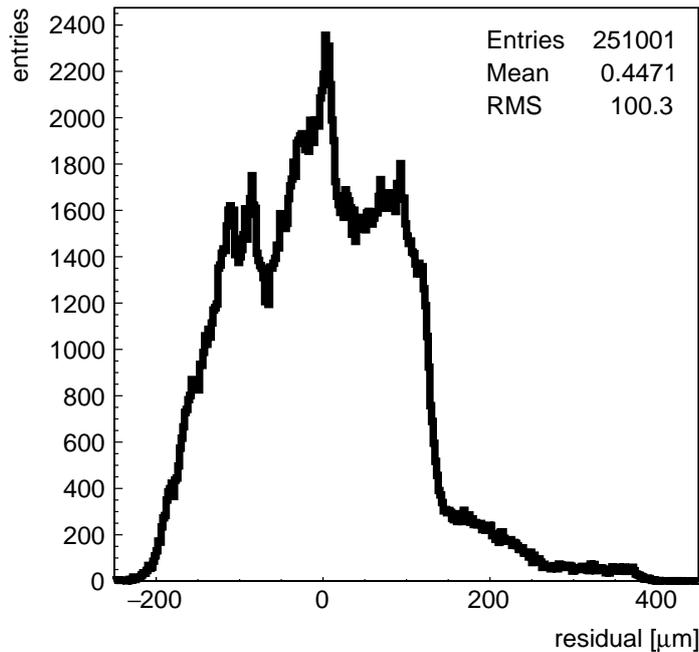

Figure 5.11: Distribution of the topology from Fig. 5.7.

By setting the topology to a minimum of 150 μm only the interference pattern remains visible, as shown in Fig. 5.12, meaning deformations of the anode are not higher than 150 μm. The lowest point of the entire active area of the detector, as shown in Fig. 5.13, can be determined at around -100 μm. The anode in the active area is planar to 250 μm. The deformation over the entire active area, a global deformation, can be removed. By assembling the detector the micro-mesh is clung to the anode. However, local deformation can not be removed as easily and can change the gain of the detector. A different distance between micro-mesh and anode modifies the width of the amplification and therefore the gain.
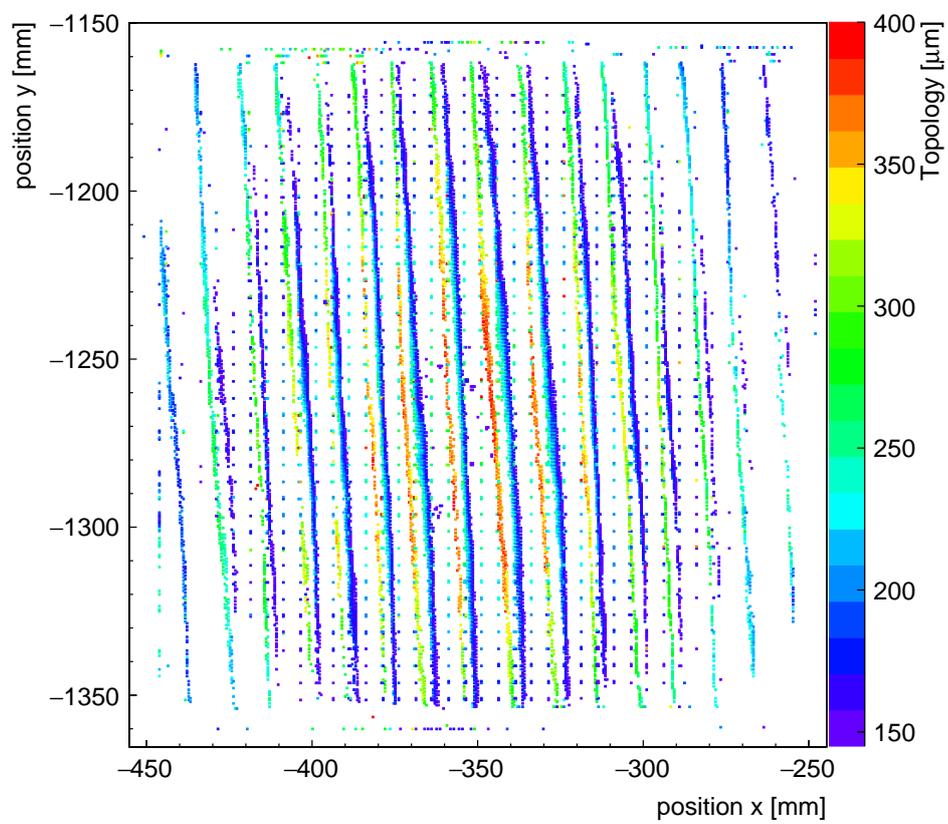
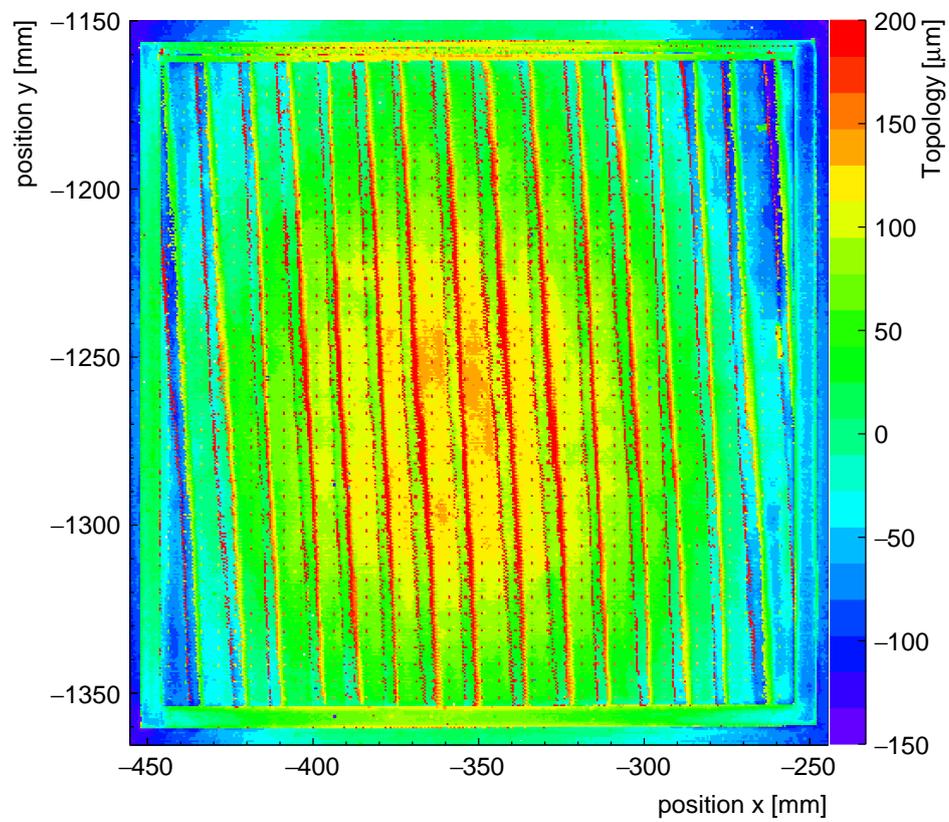Figure 5.12: Topology of the anode: By setting the minimum of 150 µm only the interference patterns and the pillars remain visible.

Figure 5.13: Topology of the anode: The lowest point of the entire active can be determined at around -100 µm. The anode in the active area is planar with a bump of 250 µm.

5.2 Assembling the Detector Components

The following work steps took place in a clean room to have no dirt present in the assembled device. O-rings, annular sealing elements made from 2.5 mm thick rubber strings, were used between single parts to seal the detector gas-tight. A gas-cover was made to seal the detector gas tight. For this 10 µm thick Kapton foil, vaporised with aluminum, was glued on an aluminum frame. A fitting piece of foil was stretched with tape, aluminum side facing down, onto a flat surface, here on a stack of paper sheet which was fixed on a table. The frame was cleaned with isopropyl and lint-free paper, lined with a thin layer of glue [UHU, 2017], put on the Kapton foil, weighed down with lead blocks and left rest for curing. After curing the foil was cut outside along the frame. Finally another layer of glue was put on along the inside of the frame to ensure proper gas-tightness. The cathode and the micro-mesh were already prepared by [Scherzer, 2016]. Following, only the main aspects of cathode and micro-mesh are described. A detailed description can be found in [Scherzer, 2016]. Similar to the gas cover, a 10 µm thick Kapton foil, vaporised with aluminum, was glued on an aluminum frame, acting together with the frame as a Faraday shield to shield the detector from possible electric fields in the surrounding area. For grounding, the foil is connected to the frame with a copper strip. The cathode, made of an aluminum-vaporized Kapton foil glued on a thin aluminum frame, is placed in the first frame. The cathode can be screwed up and down, resulting in a variable drift region. On the sides of the aluminum frame are openings for the inlet and outlet of the detector gas. A stretched stainless micro-mesh with 400 lines per inch and 25 µm wire diameter glued onto PVC bars is glued in a mesh aluminum frame, where the micro-mesh is not touching the aluminum frame. The micro-mesh is connected via a contact wire that is placed outside the detector through gas-tight holes in the metal frame and the PVC bars. Positive ions from the gas amplification drift to the mesh and thus create an electrical signal. This signal can be measured via the contact wire and used as a trigger signal for the readout electronics.

Before assembly the detector anode and micro-mesh were carefully cleaned. Large dirt residues on the anode were removed with a scalpel under the microscope. The remaining parts like cathode, gas-cover and o-rings were cleaned with isopropyl and lint-free paper. The profile of the detector is shown in Fig. 5.14. The total area of the active area is (19.2 x 19.2) cm^2.
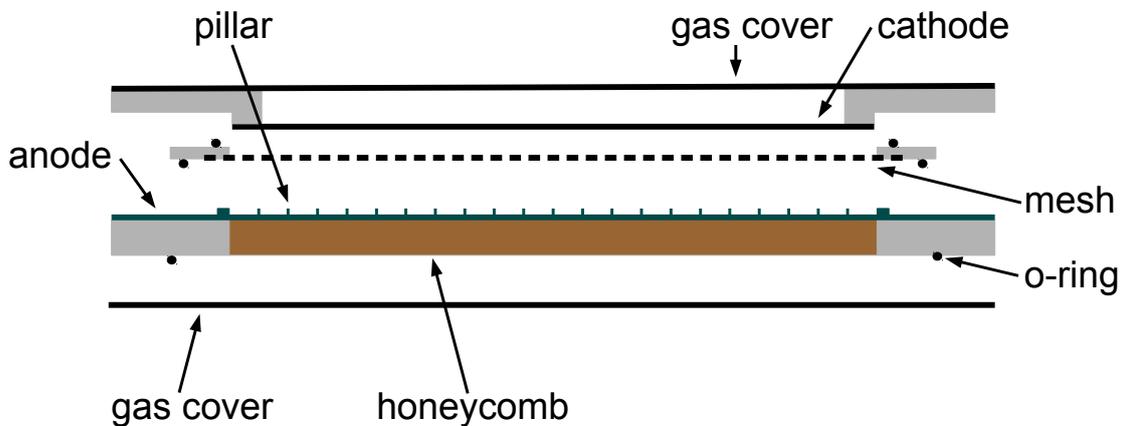

Figure 5.14: Profile of the detector. Single parts were put together to assemble the detector.

First, screws were put into the prebored holes at the corner of the gas cover frame. On this the anode was placed with a suitable o-ring in the notch on its bottom side. Two other suitable o-rings were fitted on both sides of the mesh frame, which was carefully placed on the

anode with the mesh on the bottom side. The cathode was placed on the mesh frame. The screws were slightly tightened and the remaining screws were inserted through the prebored holes. All screws were tightened diagonally to allow even pressure of the mesh on the anode. Valves for the gas supply and exhaust were screwed into the intended locations and the gas hoses attached to them.

Chapter 6

Commissioning and Characterizing Measurements of the Floating Strip Micromegas Detector

This chapter deals with the commissioning of the tested floating strip Micromegas detector, which has been described in detail in the previous chapters. The detector has an active area of $(19.2 \times 19.2)\,\mathrm{cm}^2$ and 384 anode strips, with $0.3\,\mathrm{mm}$ width and $0.5\,\mathrm{mm}$ pitch.

6.1 Measurement Setup

The measurement setup for the detector operation is described in the following. It contains the gas mixing system to flush the detector with the suitable gas mixture and the measurement setup with the readout electronics.

6.1.1 Gas Mixing System

The detector was operated with a gas mixture of $\mathrm{Ar:CO_2}$ 93:7 Vol.-% at a constant gas flow of about $2.0\,\mathrm{l/h}$ and a slight overpressure of several millibars in Munich against the standard pressure of $p_0 = 1013\,\mathrm{mbar}$ to prevent oxygen from entering the detector and reducing the spark probability. A gas mixing system was used to obtain the desired gas flow, shown in Fig. 6.1.

Gas from gas bottles with a pressure of $2\,\mathrm{bar}$ is carried into the gas flow control system by Brooks Thermal Mass Flow Controller (MFC) [Brooks Instrument, 2008], at the control of which the desired flow is set. The gas flow is measured individually on each flow control based on the specific heat capacity of the flow. The flow controls were calibrated in [Klitzner, 2016a].

The adjusted gas flow Φ_set at the gas mixing system and actual gas flow Φ_measured in the detector can be calculated [Klitzner, 2016a] with

$$\Phi_\mathrm{measured} = p_0 + p_1\,\Phi_\mathrm{set} \tag{6.1}$$

and parameters p_0 and p_1, shown in Tab. 6.1.

The gas then runs through the gas mixer and is carried into the detector. The gas runs through the amplification region, from there it reaches the drift region and finally exits the detector. Inserting a cannula in the connecting tube between drift and amplification region

induces a slight overpressure which causes a back flow due to thinner cross-section and presses the anode against the micro-mesh to obtain a constant distance of $150\,\mu m$ between micro-mesh and anode.
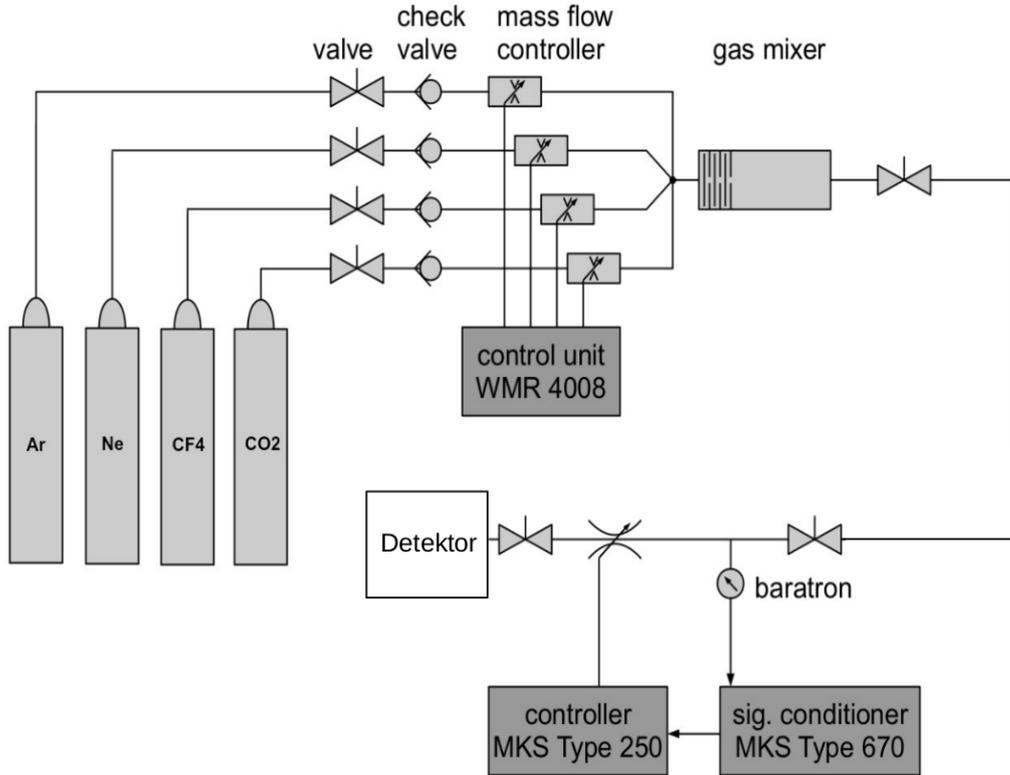

Figure 6.1: Schematic of the gas mixing system and pressure control system with connected detector. Fig. taken from [Bortfeldt, 2010] (slightly modified).

gas	MFC value	p_0	p_1
Ar	Ar	-0.04 ± 0.01	1.13 ± 0.02
Ne	N2	0.04 ± 0.02	1.58 ± 0.03
CO_2	CO_2	-0.004 ± 0.003	1.33 ± 0.04
CF4	CF4	-0.006 ± 0.008	1.07 ± 0.02

Table 6.1: Parameters for calculating the gas flow, at a pressure of $2\,bar$ [Klitzner, 2016a].

6.1.2 Readout Electronics

The measurement setup is shown in Fig. 6.2. The mesh signals were used to generate trigger signals on the signals from the individual strips of the readout layers, which were read out via APV with HDMI connection and sent directly to the PC via the front-end concentrator (FEC). The FEC digitizes the analogue APV signal with eight two-channel 12 bit analogue-to-digital-converter (ADC) units. The charge signal which is collected from the mesh is first transfered over a preamplifier and a signal splitter Fan-in/Fan-out (FiFo) to an oscilloscope. To visualize signals from noise on the oscilloscope the setup has to be grounded. A trigger threshold of $40\,mV$ is suitable. The signals are conducted from the FiFo over a timing filter amplifier (TFA), which smooths by integrating and inverts the signal. The signals from the TFA are then forwarded through the FiFo to a discriminator. The discriminator produces a

NIM-standard-logic-pulse in form of a rectangular pulse, when the pulse height exceeds an adjustable threshold. The threshold is matched to the trigger on the oscilloscope so that a logic pulse is generated only when a signal actually comes from the detector. This trigger pulse is then passed on to a dual timer, which extends the signal to the FEC. The FEC passes the trigger to the APV, which then outputs the recorded data from a time interval of 24 timebins, where 1 timbin = 25 ns, which is sent to the Computer via the FEC.
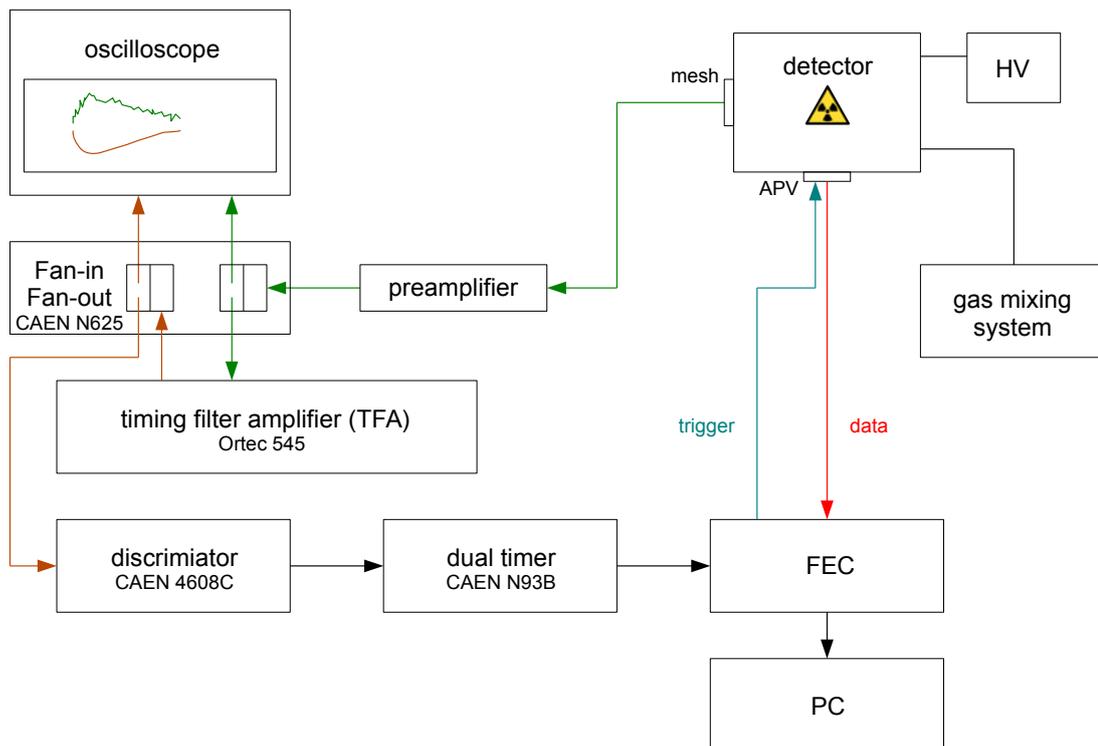

Figure 6.2: Measurement setup: The signals of the mesh (green) are transfered through the FiFo and the preamplifier to the timing filter amplifier. The shaped signal is then passed through the FiFo to the discriminator (brown), which generates a rectangular pulse therefrom, which serves as the trigger signal (blue) for the APV, which then outputs the measured signal (red).

6.2 Characterizing Measurements

In the following, characterizing measurements are presented. The detector was constantly flushed with a gas mixture of $Ar : CO_2$ $93 : 7$ vol.%. Anode and cathode were supplied with high voltage by an iseg high voltage power supply [iseg, 2017]. A ^{55}Fe source which emits low-energy 5.9 keV photons was used.

6.2.1 Variation of the Amplification Field

The pulse height is defined as the total charge of all strips in the cluster with maximum charge. Fig. 6.3 shows the recorded pulse height distribution of both readout layers as a function of

the amplification field E_{amp}. The drift field was held constantly at $E_{\mathrm{drift}} = 0.17\,\mathrm{kV/cm}$ while varying the amplification field. Clearly visible is the smaller recorded pulse height for the parallel readout layer. The most probable value of the pulse height for a given amplification field can be determined by a Gaussian fit to the distribution, Fig. 6.4 shows the most probable pulse heights for both readout layers as a function of the amplification field E_{amp}. The pulse height, which is directly proportional to the gas gain, increases in both readout layers exponentially with increasing amplification field as expected, where the pulse height in the x layer is smaller than in the y layer.
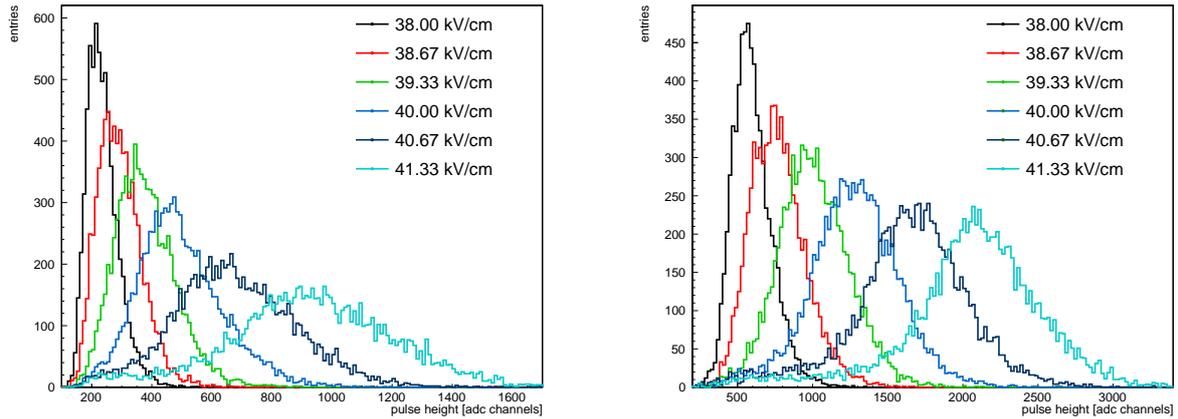

Figure 6.3: Pulse height distribution of the parallel readout layer (left) and the perpendicular readout layer (right) as a function of the amplification field E_{amp} at $E_{\mathrm{drift}} = 0.17\,\mathrm{kV/cm}$.
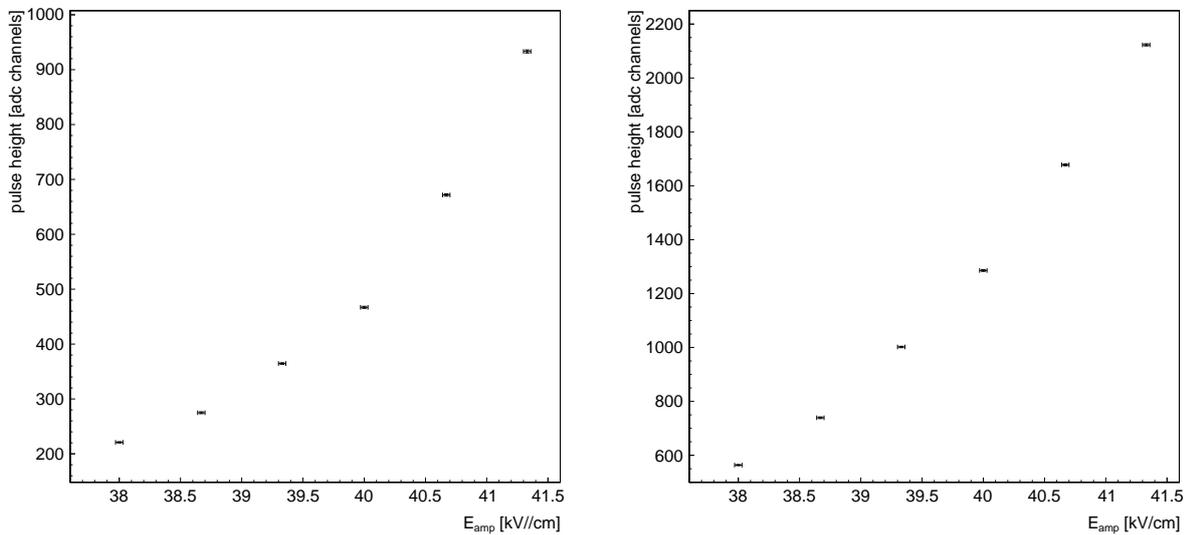

Figure 6.4: Most probable pulse height of the parallel readout layer (left) and the perpendicular readout layer (right) as a function of the amplification field E_{amp} at $E_{\mathrm{drift}} = 0.17\,\mathrm{kV/cm}$.

6.2.2   Variation of the Drift Field

The most probable pulse heights of both readout layers as a function of the drift field $E_{\mathrm{drift}}\,\mathrm{kV/cm}$ for can be seen in Fig. 6.5. The amplification field was held constant at $E_{\mathrm{amp}} = 41\,\mathrm{kV/cm}$ while varying the drift field. For increasing drift field, the pulse heights in both readout layers increase. A maximum of the most probable pulse height is reached for

$E_{\text{drift}} = 0.1\,\text{kV/cm}$. For further increasing drift field, the changing electric field configuration leads to a decrease of the measured pulse height, see also mesh transparency in section 3.3. Also here the pulse height in the x layer is smaller than in the y layer.
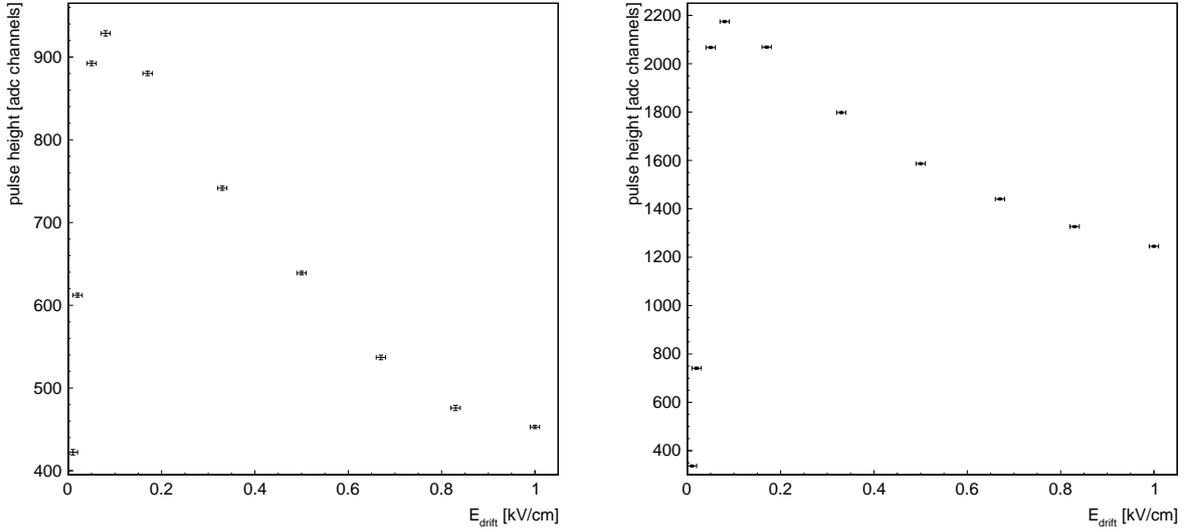

Figure 6.5: Pulse height as a function of the drift field for the parallel readout layer (left) and the perpendicular readout layer (right) at $E_{\text{drift}} = 41\,\text{kv/cm}$.

6.3 Possible Dependence of Pulse Height and Timing on the Resistance

Finally, it was examined whether the resistance value, through which the anode strips are individually connected to high voltage, affects the pulse height and the timing of detector signals. Signals of the x layer were considered for this analysis due to parallel arrangement to the anode strips. To hit several strips the ^{55}Fe source was used at different positions of the detector, resulting in three measurement recordings.

6.3.1 Relation of Pulse Height and Resistance

To determine the hit strips the pulse height of each strip is plotted against its strip number, shown in Fig. 6.6, where the entries are plotted on the z axis. Two further recordings are shown in appendix C. Visible is a localized beam spot with several hit strips. For all strips the maximum pulse height is smaller than about 1200 adc channels.
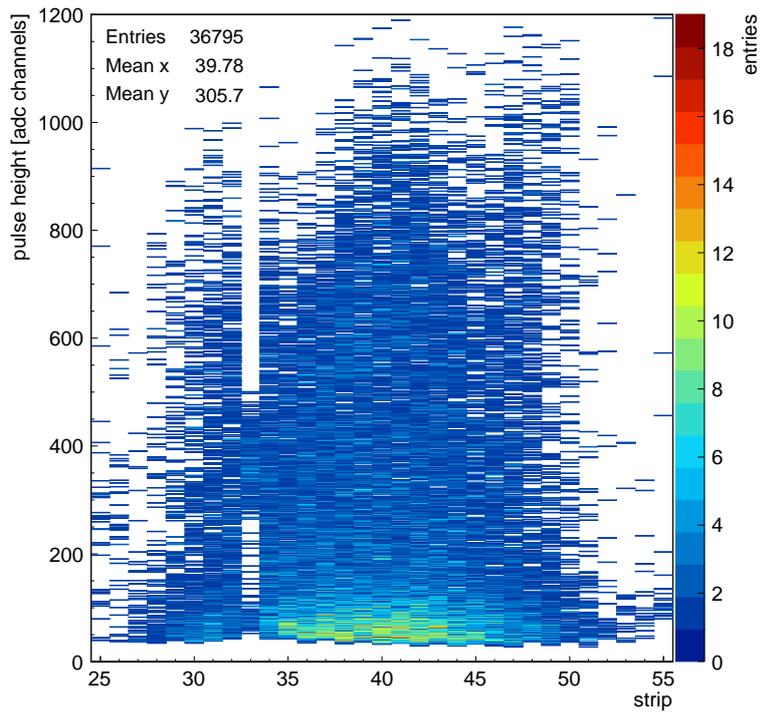
Figure 6.6: Pulse height of a strip plotted against its strip number.

For each hit strip the mean pulse height is determined with the mean of the histogram. The determined mean pulse height is plotted against its strip number, shown in Fig. 6.7. Visible is a wavelike fluctuation of the mean pulse height. This is caused by the pillar structure. The pillars are located on the anode strips and cover parts of them. As a result the active area is reduced, leading to a smaller pulse height and mean pulse height. Therefore only the mean pulse heights of several hit strips without pillars are compared and plotted against their resistances, shown in Fig. 6.8, where strips of all recordings are used. The mean pulse height fluctuates only between 330 and 360 adc channels for resistances between $4\,\text{M}\Omega$ and $20\,\text{M}\Omega$. By fitting a straight line it can be assumed that the mean pulse height is constant at (370 ± 13) adc channels for each hit strip and no trend or dependencies between pulse height and resistance can be observed.
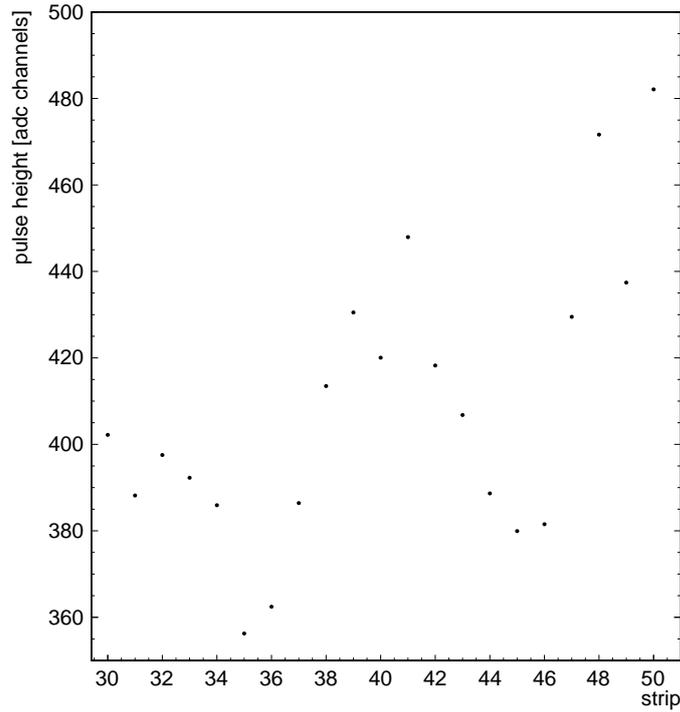
Figure 6.7: Mean pulse height of a hit strip plotted against the strip number.
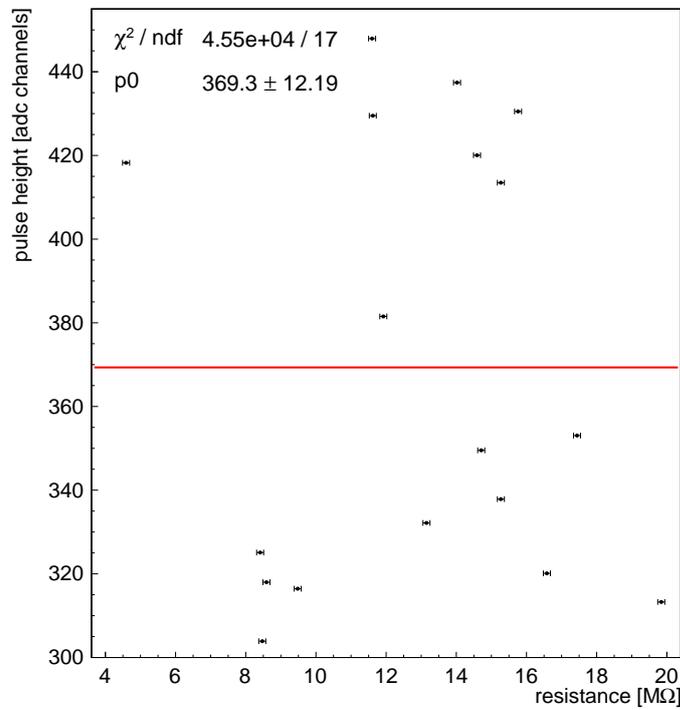

Figure 6.8: Mean pulse height of a hit strip plotted against its resistance. By fitting a straight line it can be assumed that the mean pulse height is constant at (370 ± 13) adc channels for each hit strip.

Furthermore the maximum pulse height of each hit strip was determined. A Fermi function was fitted to the falling edge of the pulse height distribution of a hit strip. Three points of the Fermi function are determined at 90%, 50% and 10% drop. A straight line is fitted through these points. The maximum pulse height can be extracted by extrapolating the straight line onto the x axis. The point of intersection with the x axis corresponds to the maximum pulse height. The maximum pulse height of each hit strip plotted against its strip number is shown in Fig. 6.9.

It has been shown that the resistance value does not affect the pulse height, shown by the mean and maximum pulse height of a hit strip.
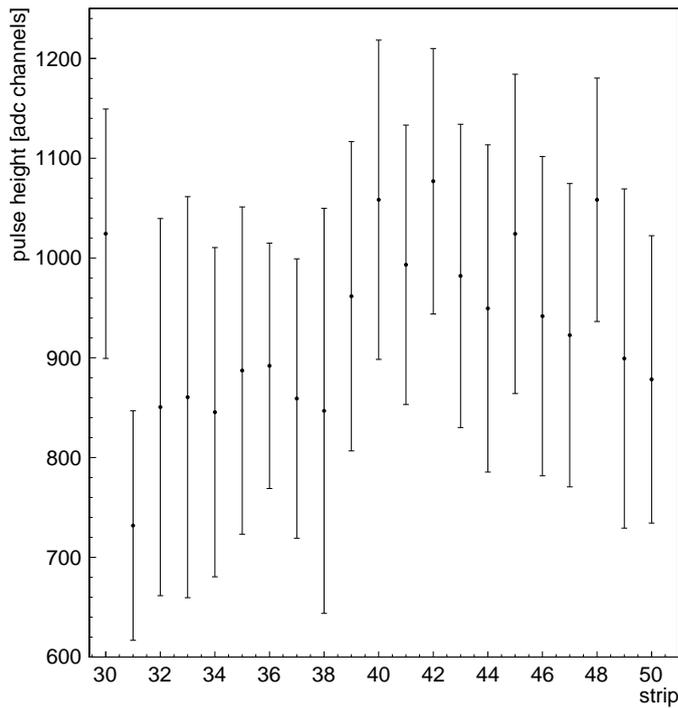

Figure 6.9: Maximum pulse height of a hit strip plotted against the strip number.
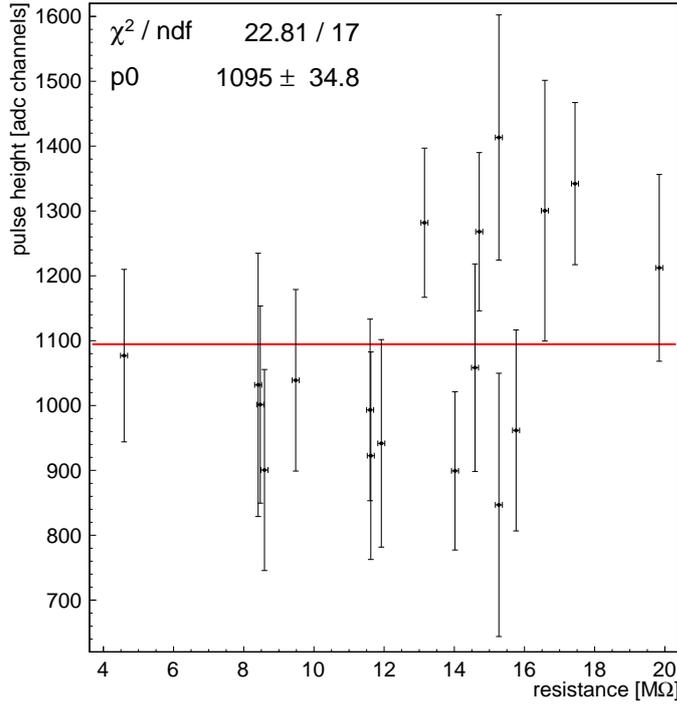
Figure 6.10: Maximum pulse height of a hit strip plotted against its resistance. By fitting a
straight line it can be assumed that the maximum pulse height is constant with (1095 ± 35) adc
channels for each strip.

6.3.2   Relation of Timing and Resistance

In addition, it was examined whether the resistance value affects the timing of detector signals.
The most probable value of the timing of a hit strip can be determined by a Gaussian fit to
the timing distribution, shown in Fig. 6.11. Fig. 6.12 shows the most probable timing of the
each hit strip plotted against its strip number.

The most probable timing of several hit strips is compared and plotted against their resis-
tances, shown in Fig. 6.13, where strips of all recordings are used. The timing fluctuates
only between 12.3 and 13.18 timebins, where a timebin equals 25 ns, for resistances between
$4\,M\Omega$ and $20\,M\Omega$. By fitting a straight line it can be assumed that the timing is constant at
(12.7 ± 0.1) timebins for each strip. Furthermore the sigma of the Gaussian timing distribu-
tion of several hit strips, the distribution for a single hit strip is shown in Fig. 6.12, is plotted
against their resistances and shown in Fig. 6.14. By fitting a straight line it can be assumed
that the sigma of the distribution is constant at (0.514 ± 0.005) timebins for each strip. It
has been shown that the resistance value does not affect the timing of a hit strip.
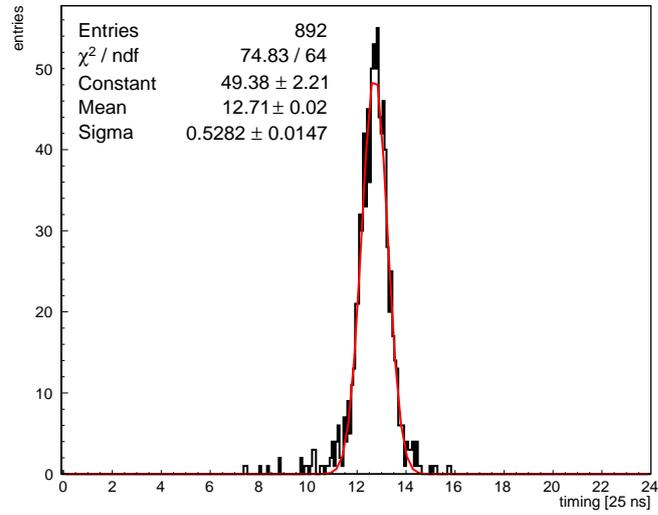
Figure 6.11: Timing distribution of a hit strip. The most probable value of the timing can be determined by a Gaussian fit.
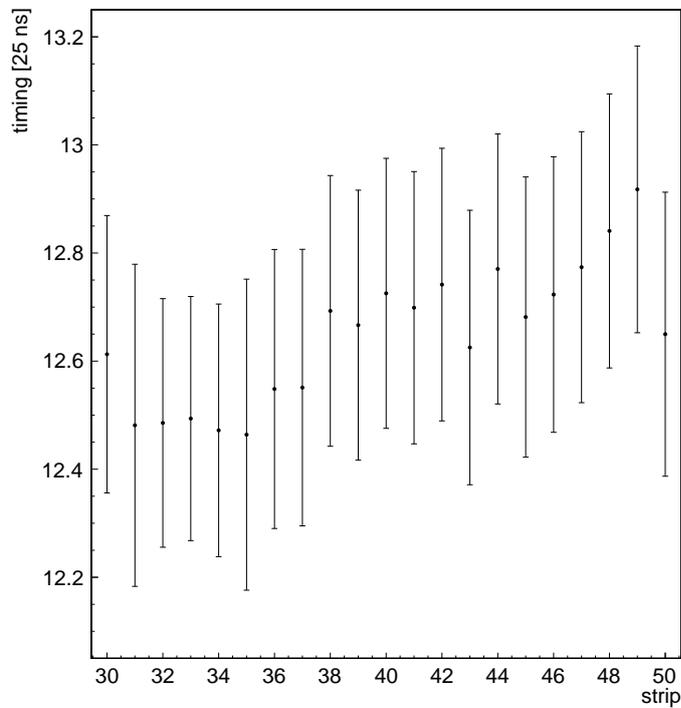
Figure 6.12: Most probable timing of a hit strip plotted against its strip number.
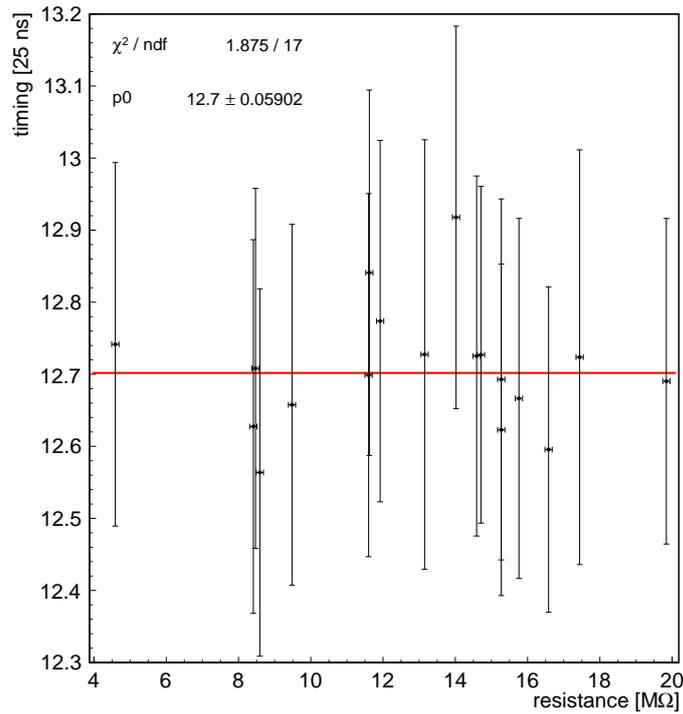
Figure 6.13: Timing of a hit strip plotted against its resistance. By fitting a straight line it can be assumed that the timing is constant at (12.7 ± 0.1) timebins for each strip, where a timebin equals 25 ns.
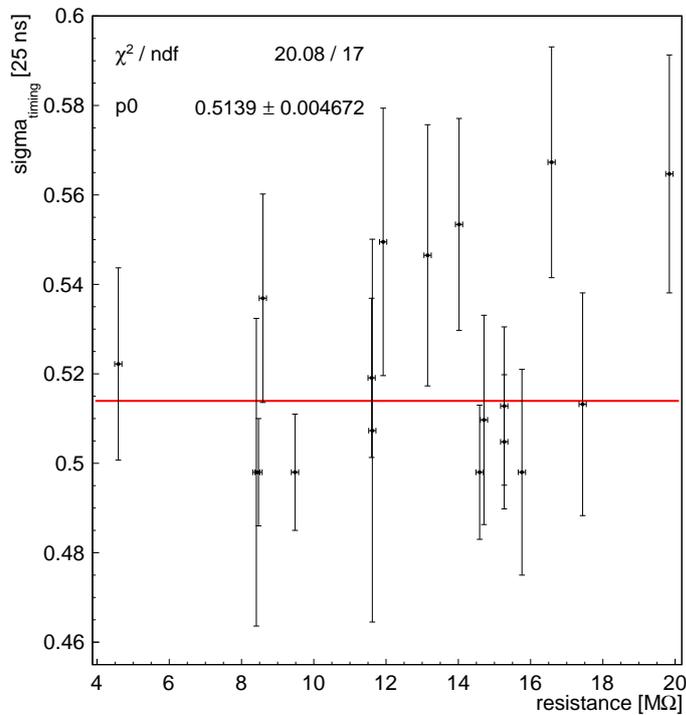
Figure 6.14: Sigma of the Gaussian timing distribution of a hit strip plotted against its resistance. By fitting a straight line it can be assumed that the sigma is constant at (0.514 ± 0.005) timebins for each strip, where a timebin equals 25 ns.

Chapter 7

Summary and Outlook

In this thesis methods for the completion of a thin anode with two-dimensional readout structure for a floating strip Micromegas detector were further developed as well as improved.

Micromgeas detectors are high-rate capable, high spatial resolution, planar gaseous detectors, consisting of individual drift and amplification regions, separated by a thin micro-mesh. The micro-mesh is held at a constant distance of $150\,\mu\text{m}$ to the anode. Charged particles or photons traverse the detector and ionize the detector gas in a typically $6\,\text{mm}$ wide drift region between cathode and micro-mesh. Created electrons drift towards the micro-mesh. In the amplification region between micro-mesh and anode these electrons are amplified in Townsend avalanches. The anode consists of copper strips. Unlike the standard Micromegas design, floating strip Micromegas use anode strips which are on a floating electrical potential due to high ohmic contact of about $20\,\text{M}\Omega$ to the high voltage supply. The generated charge is coupled to readout strips which are separated from the anode strips by a thin Kapton layer. The two-dimensional readout structure is achieved by two layers of readout strips below the anode strips, separated by a $25\,\mu\text{m}$ thin insulating Kapton layer: One orthogonal readout layer below to the anode strips, and another parallel readout layer, placed on the bottom of the PCB, separated by a $25\,\mu\text{m}$ thin insulating Kapton layer from the upper layer. Micromegas detectors are filled with a gas, typically used gas mixtures are $\text{Ar} : \text{CO}_2$ or $\text{Ne} : \text{CF}_4$.

A screen printing method, using a high polymer resistive paste, to individually connect the anode strips to high voltage was improved. A support structure was required to keep the paste in shape. After successfully building the support structure, using an improved stripping method, the resistors could be printed. To obtain suitable resistances for all anode strips, a well made support structure made out of solder resist with constant gap width is required. Desired resistances can be obtained with a suitable paste, even if the gaps are not wide open. It is necessary that the gaps are evenly wide, otherwise different amounts of paste distributed into the gaps will cause uneven resistances on individual strips. The pillar-shaped spacer structure to hold the micro-mesh at a constant distance to the anode was also made by using the stripping method. Resistors with a paste mixture of $\text{RS}12115\,_{04/11/2015}$ and $\text{RS}12115\,_{10/11/2016}$ with a ratio of $1 : 1$ for the inner gaps and a ratio of $3 : 2$ for the outer gaps and a mean resistance of $R = (11.95 \pm 3.22)\,\text{M}\Omega$ were successfully printed onto the anode.

Furthermore, the thin anode had to be supported against bending during detector operation due to gravitational sag. For this a PVC frame as well as a commercial grade aramid fiber paper honeycomb were glued onto the backside of the anode.

The topology of the anode was measured with a CMM. Results showed that a global deformation in a shape of a bump of 250 m is visible. The global deformation does not affect the functionality of the detector during operation because with assembly of the detector the micro-mesh is pressed against the anode and clings to it due to electrostatic force.

A floating strip Micromegas detector with the optimzied thin anode with two-dimensional readout structure was built with an active area of $(19.2 \times 19.2)\,cm^2$. Characterizing measurements were done using $5.9\,keV$ photons from a ^{55}Fe source. Finally, it has been shown that the resistance value, through which the anode strips are individually connected to high voltage, does not affect the pulse height and the timing of detector signals.

Bibliography

[Bichsel, 1988] Bichsel, H. (1988). Straggling in Thin Silicon Detectors. *Rev. Mod. Phys. 60:633-699.*

[Bichsel, 2006] Bichsel, H. (2006). A method to improve tracking and particle identification in TPCs and silicon detectors. *Nucl. Instr. and Meth., A562(1):154-197.*

[Bortfeldt, 2010] Bortfeldt, J. (2010). Development of Micro-Pattern Gaseous Detctors - Micromegas. Diploma thesis, Ludwig-Maximilian University Munich.

[Bortfeldt, 2014] Bortfeldt, J. (2014). Development of Floating Strip Micromegas Detectors. Phd thesis, Ludwig-Maximilian University Munich.

[Brooks Instrument, 2008] Brooks Instrument (2008). Brooks Smart Mass Flow Controllers Brooks, `http://www.brooksinstrument.com`.

[Bungard, 2017a] Bungard (2017a). Laminator RLM 419 P, `https://www.bungard.de/index.php/de/produkte/trockenresistlaminator?highlight=WyJybGOiLDQxOSwicCIsInJsbSAOMTkiLCJybGOgNDE5IHAiLCIOMTkgcCJd`, 2017-06-20.

[Bungard, 2017b] Bungard (2017b). Lötstoppmaske 3.0mil, `https://www.bungard.de/index.php/de/produkte/oberflaechen/loetstoppmaske`, 2017-06-26.

[DuPont, 2017] DuPont (2017). Pyralux PC 1025, `http://www.dupont.com/content/dam/dupont/products-and-services/electronic-and-electrical-materials/flexible-rigid-flex-circuit-materials/documents/PyraluxPC1000coverlay_DataSheet.pdf`, 2017-06-20.

[Efbe-Schott, 2017] Efbe-Schott (2017). Gesichtssolarium SC Typ 838 C, `http://www.efbe-schott.de/Wellness/Solarien/Gesichtssolarium-Wellnessbraeuner-Made-in-Germany-8-Roehren::466.html?XTCsid=frmrjablctta61hqjrrmdeg847`, 2017-06-20.

[Ellis et al., 1976] Ellis, H., Pai, R., and McDaniel, E. (1976). Transport properties of gaseous ions over a wide energy range. *Atomic Data and Nuclear Data Tables, 17:177-210.*

[ESL, 2017] ESL (2017). Polymer resitive pastes, `http://www.esleurope.co.uk/`, 2017-06-20.

[Fluke, 2000] Fluke (2000). 1520 MegOhmMeter Bedienungs-Handbuch.

[French et al., 2001] French, M. J., Jones, L. L., Morrissey, Q. R., Neviani, A., Turchetta, R., Fulcher, J. R., Hall, G., Noah, E., Raymond, M., Cervelli, G., Moreira, P., and Marseguerra, G. (2001). Design and results from the APV25, a deep sub-micron CMOS front-end chip for the CMS tracker. *Nucl. Instrum. Methods Phys. Res., A, 466(2): 359-65.*

[Giomataris et al., 1996] Giomataris, Y., Rebourgeard, P., Robert, J. P., and Charpak, G. (1996). MICROMEGAS : a high-granularity position-sensitive detector for high particle-flux environments. *Nucl.Instrum.Meth. A*, 376:29–35.

[Groom et al., 2001] Groom, D. E., Mokhov, N. V., and Striganov, S. I. (2001). Muon Stopping Power and Range Tables 10Mev - 100TeV. *Atomic Dta and Nulear Data Tables*, 78(2):183–156.

[Grupen and Shwartz, 2008] Grupen, C. and Shwartz, B. (2008). Particle Detectors. *Cambridge University Press.*

[Hubbell et al., 1980] Hubbell, J. H., Gimm, H. A., and Øverbo, I. (1980). Pair, Triplet, and Total Atomic Cross Sections (and Mass Attenuation Coefficient) for 1 MeV - 100 GeV Photons in Elements Z = 1 to 100. *Jour. of Phys. and Chem. Ref. Data, 9(4):1023-1147.*

[iseg, 2017] iseg (2017). High Precision HV Supply SHQ, `http://iseg-hv.com/de/products/detail/SHQ`, 2017-06-20.

[Kleinknecht, 1992] Kleinknecht, K. (1992). *Detektoren für Teilchenstrahlung.* Teubner, Stuttgart.

[Klitzner, 2016a] Klitzner, F. (2016a). Private conversation.

[Klitzner, 2016b] Klitzner, F. (2016b). Studies of Floating Strip Micromegas Detectors in Proton and Carbon Ion Beams with a Fast Gas Mixture. Master thesis, Ludwig-Maximilian University Munich.

[Klitzner et al., 2016] Klitzner, F., Biebel, O., Flierl, B., Hertenberger, R., Lösel, P., and Bortfeldt, J. (2016). Novel Two-Dimensional Floating Strip Micromegas Detectors. *PoS(ICHEP2016)1190.*

[Leo, 1994] Leo, W. R. (1994). *Techniques for Nulear and Particle Physics Experiments.* Springer, second edition.

[Mirco-Epsilon, 2017] Mirco-Epsilon (2017). Blue Laser Triangulation Displacement Sensor optoNCDT2300-2BL, `http://www.micro-epsilon.com/download/products/_laser-sensor/dax--optoNCDT-2300BL--en-us.html`, 2017-06-26.

[Müller, 2017] Müller, R. (2017). Quality Control of Micromegas Detectors for the ATLAS New Small Wheel Upgrade Project and Optimization of the Spatial Resolution of PoSSuMus Detectors in two Dimensions. Phd thesis, Ludwig-Maximilian University Munich.

[Panasonic, 2017] Panasonic (2017). Panasonic Electric Works AXK5SA3277YG CONN SOCKET BRD/BRD .5MM 130POS, `https://www.panasonic-electric-works.com/eu/`, 2017-06-26.

[Raether, 1964] Raether, H. (1964). *Electron Avalanches and Breakdown in Gases.* Butterworths, London.

[Raizer, 1991] Raizer, Y. P. (1991). *Gas Discharge Physics.* Springer, Berlin Heidelberg.

[Scherzer, 2016] Scherzer, J. (2016). Development and Commisioning of a Thin 2-dimensional Floating Strip Micromegas Detector with Modified Anode Structure.

[UHU, 2017] UHU (2017). UHU plus endfest 2-K-Epoxidharzkleber, `http://www.uhu.com/de/produkte/2-komponenten-klebstoffe/detail/uhu-plus-endfest-3002-k-epoxidharzkleber.html?step=84&cHash=6e79ee42e24cb8747ce7afc7b5654f02`, 2017-06-20.

Appendix A

Technical Specifications for Printing High Ohmic Resistors by Using a Screen Printing Method

Settings for the Laminator RLM 419 P

- speed: $0.9\,\mathrm{m/s}$
- temperature: about $100\,^\circ\mathrm{C}$
- pressure: 4-5 (from max. 6) device specific scale, adjustable via hand wheel

ESL EUROPE
8 COMMERCIAL ROAD
READING, ENGLAND
RG2 0QZ
T: +44 (0) 118 9182400
F: +44 (0) 118 9867331
sales@esleurope.co.uk

Product Manufactured
under the Quality System
ISO 9001:2008 Cert. No. 28823
and the Environmental
Management System
ISO 14001:2004 Cert. No. 28831
Approved by URS

POLYMER RESISTOR CERTIFICATION AND DATA

RoHS Compliant*

We certify that the product identified below has been manufactured and inspected in compliance with the requirements of the mutually accepted specifications of your purchase order. We further certify that the applicable test reports are on file and available for examination as appropriate.

This product was manufactured at the above location and is certified to have a shelf life of six (6) months from the date of shipment when stored in a closed container and refrigerated at 5°C. However, no warranty is expressed or implied regarding the suitability of this product for any specific purpose.

Andrew Sale
Product Manufacturing Manager

Michele Bond
Quality Manager

DATE OF APPROVAL: 4 November 2015

TEST DATA

PRODUCT No.   RS12116   **LOT No.**   K743-95   **SPECIFICATION No.**   UK-2

VISCOSITY (Pa.s):
(Brookfield RVT/ No.7 Spindle)   72   @ 10 rpm,   62   @ 50 rpm,   ---   @ 100 rpm, @ 25.2   °C

CURED THICKNESS: 18.0   µm cured @   150°C / 2 hours   with   1109-S   terminations

RESISTIVITY: 1212.8   KΩ/☏ on 5 mm x 5 mm square resistor

SOLIDS: 69.0   %

APPEARANCE: ACCEPTABLE

RoHS
COMPLIANT

*None of the six substances referred to in the RoHS Directive (2002/95/EC) are used in the formulation of this product.

Form 29 / Mar 08

Figure A.1: Polymer resistive paste RS12116 by ESL with $1212.8\,\mathrm{k\Omega/sq}$ resistivity on a (5 x 5)$\,\mathrm{mm^2}$ square.

ESL EUROPE
8 COMMERCIAL ROAD
READING, ENGLAND
RG2 0QZ
T: +44 (0) 118 9182400
F: +44 (0) 118 9867331
sales@esleurope.co.uk

Product Manufactured
under the Quality System
ISO 9001:2008 Cert. No. 28823
and the Environmental
Management System
ISO 14001:2004 Cert. No. 28831
Approved by URS

POLYMER RESISTOR CERTIFICATION AND DATA

RoHS Compliant*

We certify that the product identified below has been manufactured and inspected in compliance with the requirements of the mutually accepted specifications of your purchase order. We further certify that the applicable test reports are on file and available for examination as appropriate.

This product was manufactured at the above location and is certified to have a shelf life of six (6) months from the date of shipment when stored in a closed container and refrigerated at 5°C. However, no warranty is expressed or implied regarding the suitability of this product for any specific purpose.

Andrew Sale
Product Manufacturing Manager

Michele Bond
Quality Manager

DATE OF APPROVAL: 4 November 2015

TEST DATA

PRODUCT No.   **RS12115**   **LOT No.**   **K749-2**   **SPECIFICATION No.**   **UK-2**

VISCOSITY (Pa.s):   62   @ 10 rpm,   38   @ 50 rpm,   33   @ 100 rpm,   @   25.3   °C
(Brookfield RVT/ No.7 Spindle)

CURED THICKNESS: 18.0   µm cured @   150°C / 2 hours   with   1109-S   terminations

RESISTIVITY: 96.9   KΩ/☎ on 5 mm x 5 mm square resistor

SOLIDS: 64.3   %

APPEARANCE: ACCEPTABLE

RoHS
COMPLIANT

*None of the six substances referred to in the RoHS Directive (2002/95/EC) are used in the formulation of this product.

Form 29 / Mar 08

Figure A.2: Polymer resistive paste RS12115 by ESL with $96.9\,\mathrm{k\Omega/sq}$ resistivity on a $(5 \times 5)\,\mathrm{mm^2}$ square.

ESL EUROPE
8 COMMERCIAL ROAD
READING, ENGLAND
RG2 0QZ
T: +44 (0) 118 9182400
F: +44 (0) 118 9867331
sales@esleurope.co.uk

Product Manufactured
under the Quality System
ISO 9001:2008 Cert. No. 28823
and the Environmental
Management System
ISO 14001:2004 Cert. No. 28831
Approved by URS

POLYMER RESISTOR CERTIFICATION AND DATA

RoHS Compliant*

We certify that the product identified below has been manufactured and inspected in compliance with the requirements of the mutually accepted specifications of your purchase order. We further certify that the applicable test reports are on file and available for examination as appropriate.

This product was manufactured at the above location and is certified to have a shelf life of six (6) months from the date of shipment when stored in a closed container and refrigerated at 5°C. However, no warranty is expressed or implied regarding the suitability of this product for any specific purpose.

Andrew Sale
Product Manufacturing Manager

Michele Bond
Quality Manager

DATE OF APPROVAL: 10 November 2016

TEST DATA

PRODUCT No. **RS12115**   **LOT No.**   **K765-92**   **SPECIFICATION No.**   **UK-2**

VISCOSITY (Pa.s): (Brookfield RVT/ No.7 Spindle)   61   @ 10 rpm,   33   @ 50 rpm,   31   @ 100 rpm, @   26.0   °C

CURED THICKNESS: 18.8   µm cured @   150°C / 2 hours   with   1109-S   terminations

RESISTIVITY: 84.9   KΩ/☎ on 5 mm x 5 mm square resistor

SOLIDS: 62.3   %

APPEARANCE: ACCEPTABLE

RoHS
COMPLIANT

*None of the six substances referred to in the RoHS Directive (2002/95/EC) are used in the formulation of this product.

Form 29 / Mar 08

Figure A.3: Polymer resistive paste RS12115 by ESL with $84.9 \, \mathrm{k\Omega/sq}$ resistivity on a (5 x 5) mm^2 square.

Appendix B

Technical Specifications for Soldering the Panasonic Connectors

Heating Elements

- Ceramic Cartridge Heater for RepRap 3D printer
- stainless steel core and copper plated tube (model N/A)
- size: 6 mm diameter and 20 mm length
- 40 W power and operating voltage between 12 V and 24 V voltage
- five heating elements:
    - two elements were operated together with 20 V
    - three elements were operated together with 20 V

Appendix C

Additional recordings of Pulse Height and Timing Relations

Fig. C.1 shows the pulse height of a strip plotted against its strip number for two further recordings. For hit strips mean pulse height and maximum pulse height are determined and plotted against the strip number, shown in Fig. C.2 and Fig. C.3 The timing plotted against the strip number is shown in Fig. C.4.
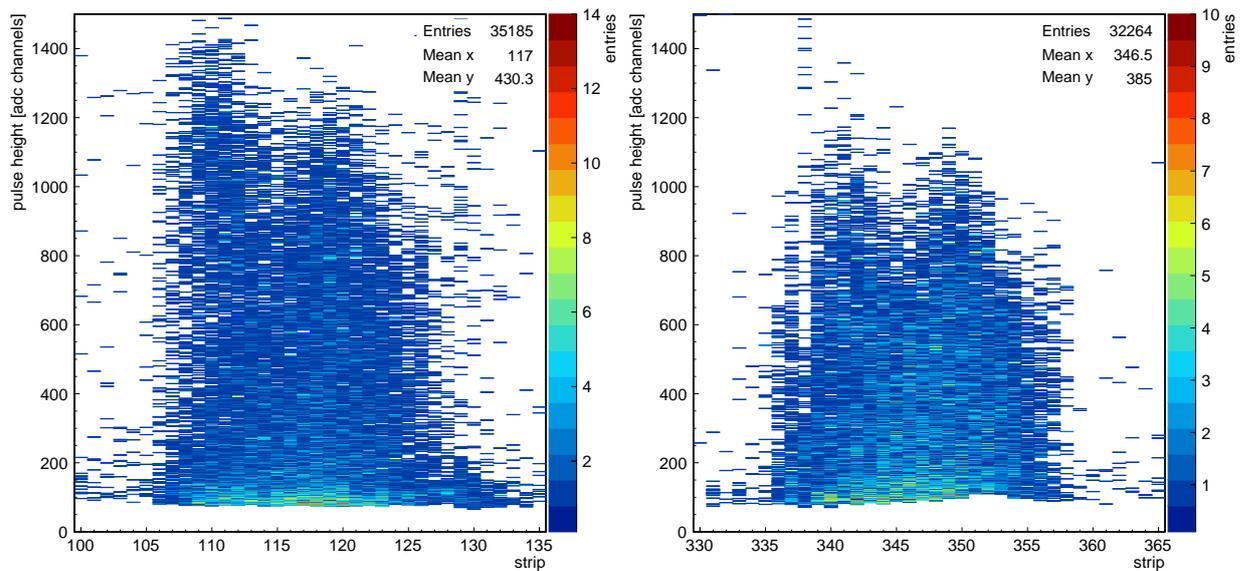

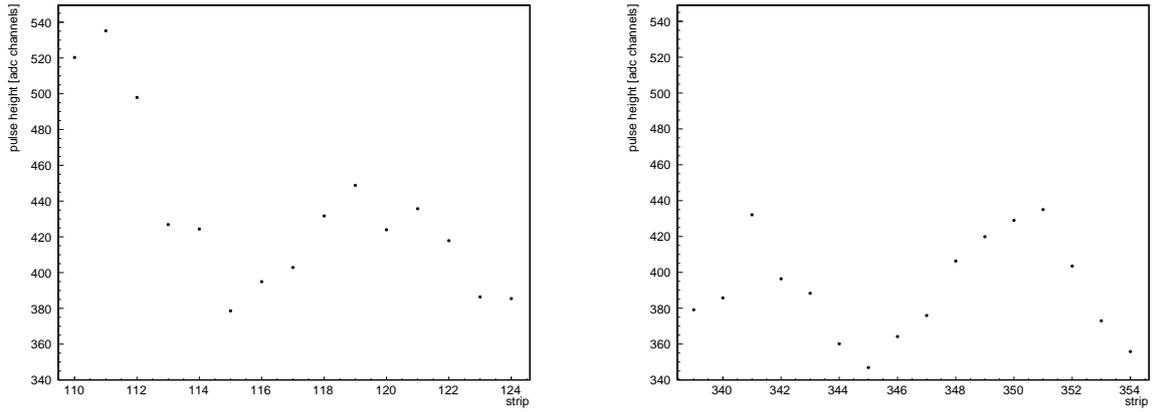Figure C.1: Pulse height of a strip plotted against its strip number.

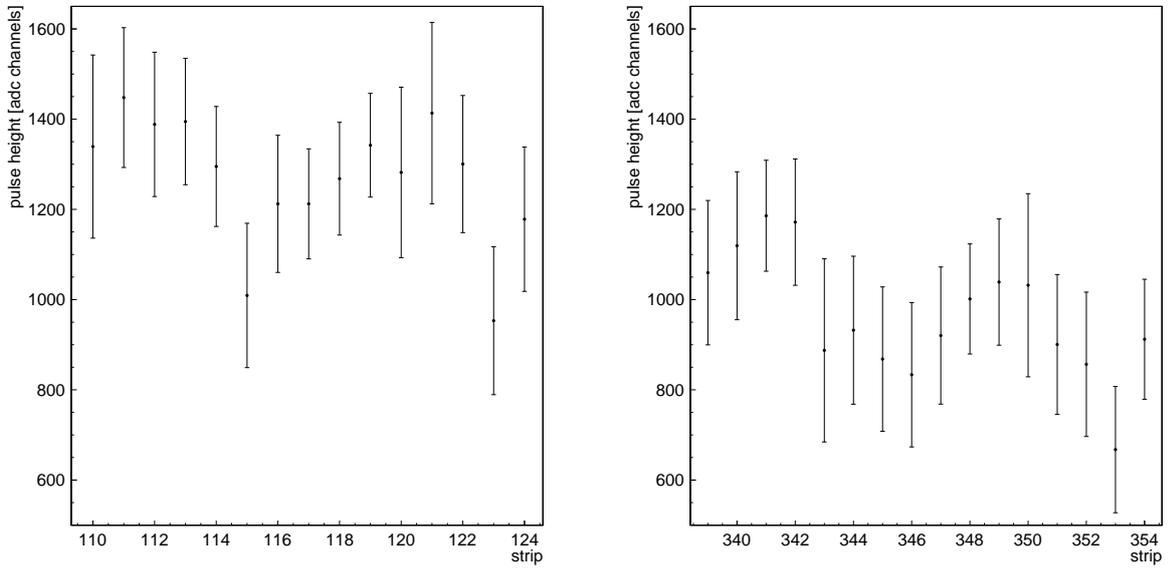Figure C.2: Mean pulse height of a hit strip plotted against the strip number.

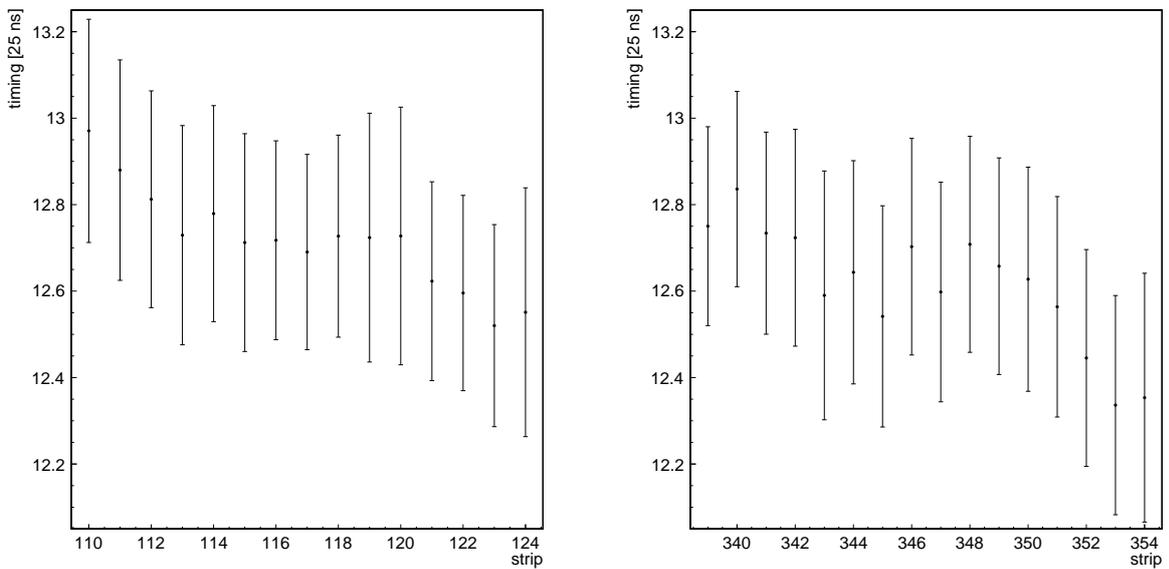Figure C.3: Maximum pulse height of a hit strip plotted against the strip number.

Figure C.4: Timing of a hit strip plotted against the strip number.

Selstständigkeitserklärung

Hiermit erkläre ich, die vorliegende Arbeit mit dem Titel

**Printing High Ohmic Resistors and Improvement of a Thin Anode for
Two-dimensional Floating Strip Micromegas Detectors**

selbständig verfasst zu haben und keine anderen als die in der Arbeit angegebenen Quellen
und Hilfsmittel benutzt zu haben.

Isabel Frank

München, den 14. September 2017